

Structure of alpha-synuclein fibrils derived from human Lewy body dementia tissue

Dhruva D. Dhavale^{1,13}, Alexander M. Barclay^{2,13}, Collin G. Borcik³, Katherine Basore⁴, Deborah A. Berthold⁵, Isabelle R. Gordon¹, Jialu Liu¹, Moses H. Milchberg³, Jennifer Y. O'Shea¹, Michael J. Rau⁴, Zachary Smith¹, Soumyo Sen⁶, Brock Summers⁴, John Smith⁷, Owen A. Warmuth³, Richard J. Perrin^{1,8}, Joel S. Perlmutter^{1,9}, Qian Chen⁷, James A. J. Fitzpatrick⁴, Charles D. Schwieters¹⁰, Emad Tajkhorshid⁶, Chad M. Rienstra^{2,3,11,12,14@}, Paul T. Kotzbauer^{1,14@}

¹Department of Neurology and Hope Center for Neurological Disorders, Washington University School of Medicine, St. Louis, MO 63110, USA

²Center for Biophysics and Quantitative Biology, University of Illinois at Urbana-Champaign, Urbana, IL 61801, USA

³Department of Biochemistry, University of Wisconsin-Madison, Madison, WI 53706, USA

⁴Center for Cellular Imaging, Washington University School of Medicine, St. Louis, MO 63110, USA.

⁵Department of Chemistry, University of Illinois at Urbana-Champaign, Urbana, IL 61801, USA

⁶Theoretical and Computational Biophysics Group, NIH Resource for Macromolecular Modeling and Visualization, Beckman Institute for Advanced Science and Technology, Department of Biochemistry, and Center for Biophysics and Quantitative Biology, University of Illinois at Urbana-Champaign, Urbana, IL 61801, USA.

⁷Department of Materials Science and Engineering, University of Illinois at Urbana-Champaign, IL 61801, USA

⁸Department of Pathology & Immunology, Washington University School of Medicine, St. Louis, MO 63110, USA

⁹Department of Radiology, Neuroscience, Physical Therapy and Occupational Therapy, Washington University School of Medicine, St. Louis, MO 63110, USA

¹⁰Computational Biomolecular Magnetic Resonance Core, National Institute of Diabetes and Digestive and Kidney Diseases, National Institutes of Health, Bethesda, MD 20892, USA

¹¹Morgridge Institute for Research, University of Wisconsin-Madison, Madison, WI 53706 USA

¹²National Magnetic Resonance Facility at Madison, University of Wisconsin-Madison, Madison, WI 53706, USA

¹³These authors contributed equally: Dhruva D. Dhavale, Alexander M. Barclay

¹⁴These authors jointly supervised this work: Chad M. Rienstra, Paul T. Kotzbauer

@Correspondence to crienstra@wisc.edu and kotzbauerp@wustl.edu

Supplementary Information

Supplementary Notes 1: Chemical Shift Assignments

Chemical shift assignments were performed for the LBD tissue-derived Asyn fibril using two independently produced samples — one with uniform [^{13}C , ^{15}N] labeling (uCN) and a second with uniform [^{13}C , ^2H , ^{15}N] labeling (uCDN) followed by back-exchange in 99.8% D_2O after fibril amplification done in 100% H_2O . Resonance assignments for the uCN sample were determined using 2D ^{13}C - ^{13}C , 3D ^{15}N - $^{13}\text{C}\alpha$ - $^{13}\text{C}\text{X}$, 3D ^{15}N - $^{13}\text{C}'$ - $^{13}\text{C}\text{X}$, and 3D $^{13}\text{C}\alpha$ - ^{15}N - $^{13}\text{C}'$ data sets following standard procedures^{1,2}. The complete list of data sets used for performing assignments using ^{13}C -detection is presented in Supplementary Table 9 and ^{13}C - ^{15}N resonance assignments have been reported in the BioMagRes Bank (BMRB accession code 51678)³. The 2D ^{13}C - ^{13}C spectrum serves as a conformational fingerprint of the fibril and provides some initial insights into the structure (Fig. 4a). Globally, the resolved peaks display decoupled line widths of < 0.4 ppm in the direct ^{13}C dimension, similar to those observed for in vitro Asyn fibrils and indicative of a highly ordered core^{4,5}. Particular residue types including most Thr, Val, and Gly residues, as well as select spin systems from other residues such as L38, N65, Q79, S87, I88, and F94, are particularly well resolved in the 2D. The Lys and Glu regions, which account for 20% of the primary sequence between residues 30 and 100, are less well resolved than in the in vitro forms, indicating disorder or partial mobility for some of these residues. In contrast to the in vitro form, the Ala regions are less well resolved in the 2D ^{13}C - ^{13}C , but the signals have comparable intensity to the resolved regions, indicating a high degree of order consistent with beta-strand conformations. Interestingly, some conformational disorder is evident for S87 and I88. The 2D ^{15}N - $^{13}\text{C}'$ and ^{15}N - $^{13}\text{C}\alpha$ spectra also serve as structural fingerprints for the fibril, with a focus on the backbone atoms (Supplementary Fig. 12). Critically, these highlight the benefit of adding a ^{15}N dimension to disambiguate shifts, particularly for the Ala and Gly regions, which comprise 30% of the primary sequence between residues 30 and 100, as well as for key core residues like V71, V74, T75, and V77. Overall, there appears to be a predominant defined conformation that exhibits some localized heterogeneity.

Resonance assignments for the uCDN sample were determined using 3D ^1H -detection experiments including $^{13}\text{C}\alpha$ - ^{15}N - ^1H , $^{13}\text{C}'$ -($\text{C}\alpha$)- ^{15}N - ^1H , $^{13}\text{C}'$ - ^{15}N - ^1H , and $^{13}\text{C}\alpha$ -(C')- ^{15}N - ^1H and performed as described^{2,6}. The complete list of data sets used for performing assignments using ^1H -detection is presented in Supplementary Table 9. The benefits of using ^1H -detection are: (1) the sensitivity is approximately four-fold greater than for ^{13}C -detection, (2) the amide ^1H chemical shift can be used in conjunction with backbone ^{13}C and ^{15}N shifts for predicting phi and psi dihedral angles, (3) in the presence of D_2O as the hydration liquid, signals only arise from ^1H s participating in hydrogen bonding, (4) it provides an independent method for determining the backbone chemical shift assignments that is complementary to the ^{13}C -detection methods. In addition, ^{13}C -detection can still be utilized for performing a 2D ^{13}C - ^{13}C fingerprint analysis (Supplementary Fig. 12a-b). As denoted by the labels, the peak patterns are identical to those of the uCN sample, demonstrating the fidelity of the amplification protocol. This similarity is also evident from the 2D ^{15}N - $^{13}\text{C}'$ and ^{15}N - $^{13}\text{C}\alpha$ projections from the 3D $^{13}\text{C}\alpha$ - ^{15}N - ^1H and $^{13}\text{C}'$ - ^{15}N - ^1H experiments (Fig. 4b). In addition to confirming the backbone ^{13}C and ^{15}N assignments determined for the uCN sample, additional assignments were made for residues K43, Q62, E83, G84, A85, and G86, which gave better-

resolved data in the ^1H -detected experiments than in the ^{13}C -detected 3Ds. All ^{13}C and ^{15}N atoms with unambiguous assignments from either or both samples are summarized as filled black circles on the primary sequence (Supplementary Fig. 12), with the corresponding chemical shift assignments in Supplementary Table 10.

Backbone phi and psi dihedral angles were predicted using assignments for ^{15}N , $^{13}\text{C}\alpha$, $^{13}\text{C}'$, $^{13}\text{C}\beta$, and $^1\text{H}^N$ using TALOS-N⁷, and are consistent with a primarily beta-strand secondary structure (Fig. 4d). Relative peak intensities in a CP experiment provide a qualitative indicator of the relative rigidity for the different regions. This is plotted for the 3D $^{13}\text{C}\alpha$ - ^{15}N - ^1H data (Fig. 4d), and in conjunction with the TALOS-N results, suggest a protomer structure composed of five beta-strands. Since the uCDN sample was back-exchanged in D_2O after seed amplification, the weaker peaks in the ^1H -detected data suggests residues that could be in loops or turns that are otherwise rigid, but not involved in strong backbone hydrogen bonding and may exchange slowly with the D_2O hydrating liquid. Using the same logic, the residues that show strong peaks in the ^1H -detected data must be participating in backbone hydrogen bonding between beta-strands.

Distance restraints from solid-state NMR

The next step towards determining the structural fold of the LBD Asyn fibril was to detect medium- ($2 \leq |i-j| \leq 4$) and long-range ($|i-j| \geq 5$) distance correlations to be used as restraints in a structure calculation. We performed measurements of distances using pulse sequences that minimize the effects of dipolar truncation⁸ such as PAR⁹. This sequence takes advantage of a proton-drive second-order polarization transfer mechanism that is resilient to dipolar truncation and has been demonstrated to generate high-quality distance restraints for structure determinations of several proteins including a uniform [^{13}C , ^{15}N] labeled amyloid-beta fibril¹⁰. Here, PAR mixing was incorporated into a 2D ^{13}C - ^{13}C pulse sequence and used to detect medium- and long-range correlations in the uCN LBD fibril sample (Supplementary Fig. 13). In comparison to the spectrum in Fig. 4, which was collected with 75 ms DARR mixing¹¹, the 12 ms PAR spectrum displays significantly more intensity arising from the medium and long-range correlations, which encode the highest value structural information. Even the 2D spectrum exhibits a number of well resolved strips that have an unambiguous assignment in one dimension, including I88CD1, I88CG2, V70CB, G73CA, L38CA, S87CB, K43C, V66C, and Q79CD. Additionally, a substantial set of peaks have only two possible assignments in one dimension, including L38CD1 or V77CG2, L38CG or I88CG1, V74CB or Q79CB, N65CB or Lys CE, L38CB or G67CA, N65CA or H50CA, and G41C or G93C. Many additional correlations were observed but could not be assigned from the 2D spectrum alone.

To disambiguate some of the other regions of spectral overlap, PAR mixing was incorporated into 3D pulse sequences (Supplementary Fig. 14). We employed a modification of the 3D ^{13}C - ^{13}C - ^{13}C pulse sequence from Hong and co-workers,¹² utilizing RFDR^{13,14} for the first mixing period to maximize the intensity of one-bond correlations and then PAR transfer during the second mixing period to detect long-range correlations. This combination of mixing elements gave especially strong and well-resolved signals for Gly, Ala, Thr, Val, Asn, and Gln residues. We also employed a related 3D ^{15}N - ^{13}C - ^{13}C pulse sequence¹⁵ utilizing constant-time evolution¹⁶ in the ^{15}N dimension to provide resolution enhancement, followed by SPECIFIC CP¹⁷ to transfer magnetization selectively to either the $\text{C}\alpha$ or C' spectral regions prior to PAR transfer between ^{13}C s. Both

sequences utilized non-uniform sampling (NUS) and SMILE processing of the two indirect dimensions¹⁸⁻²⁰, reducing experimental times and enhancing the resolution and sensitivity, while allowing broadband sampling of all three ¹³C dimensions.

Several long-range correlations were identified in the 2D ¹³C-¹³C experiment by exploiting the unambiguously assigned strips in the indirect dimension (Supplementary Fig. 15a). Substantial portions of the spectra could be assigned uniquely as a validation of the data quality. For example, we assigned correlations from L38CA to A78CA/CB; V70CB to N65CA/CB; and G73CA to F94CD. Additionally, T92CB and T72CB are clearly resolved in the 3D ¹³C-¹³C-¹³C and independently exhibit distinct cross peaks with F94CD (Supplementary Fig. 15b). The 2D also reveals cross-peaks from S87CB to either A78CA or A91CA, as well as multiple cross-peaks between the I88 methyl groups and the Q79 and V77 spin systems. Additional correlations from the 3D ¹³C-¹³C-¹³C include cross peaks between the G41CA and A69CA/CB and V70CB; N65CB and V70CA/CB/CG; G68CA to S42CA/CB and G41C; T75CB to T92CB; and T92CB to V74C'/CA/CB and G73C'. Finally, the 3D ¹⁵N-¹³C α -¹³CX resolves additional cross peaks between S42CA and A69CA/CB and G68C'; A69CA and S42CA/CB and G41C'; V74CA and T92CB; and A78CA to L38, G36CA, and I88CG2.

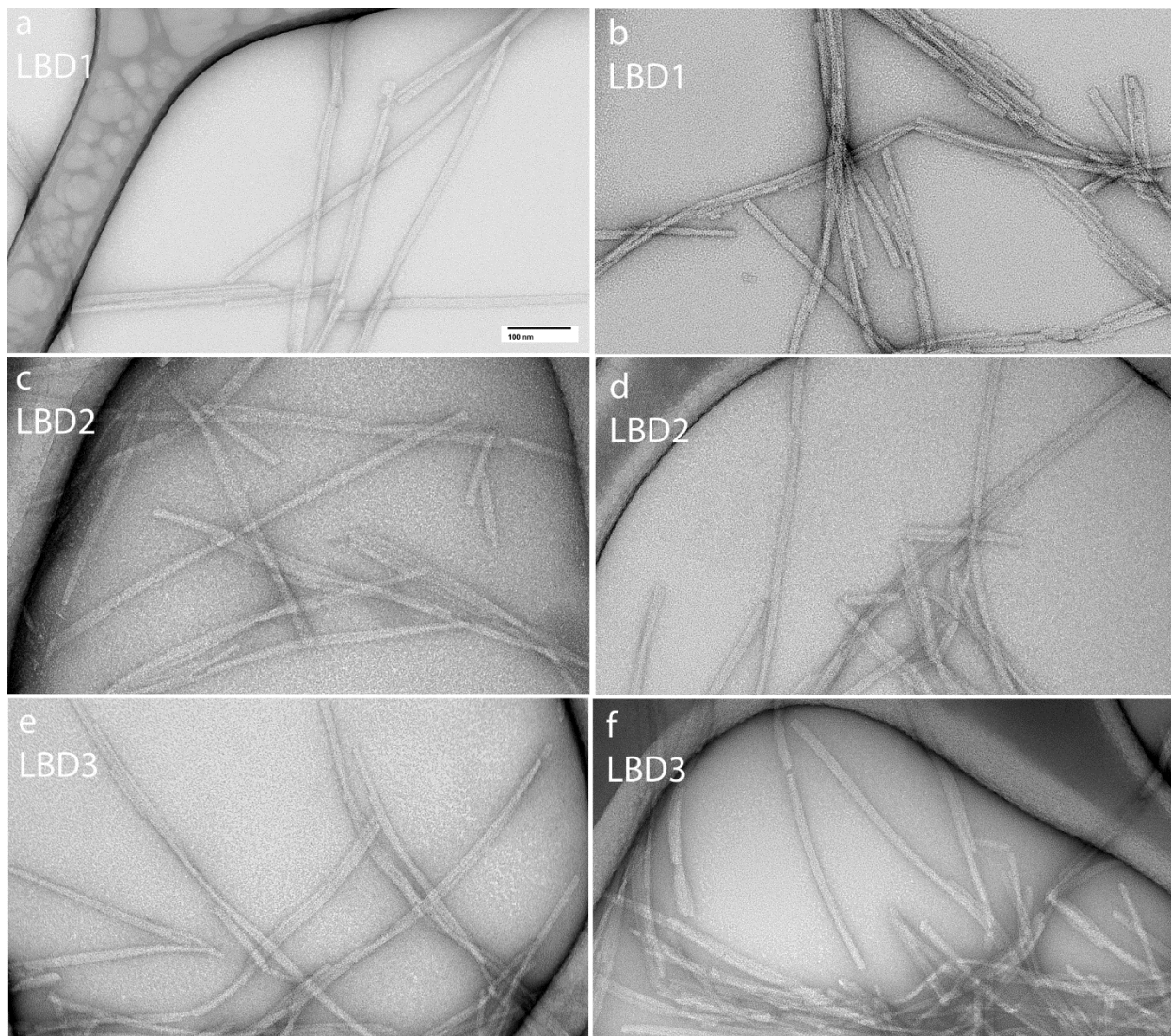
In addition to the distance restraints generated using the uCN sample, a third sample was prepared using isotopic dilution; Asyn monomer prepared with a [2-¹³C]-glycerol, uniform-¹⁵N labeling pattern was diluted approximately four-fold in natural abundance monomer prior to fibril amplification (diluted). The advantage of this sample was that long-range cross-peaks in a 2D ¹³C-¹³C correlation experiment arise primarily from *intramolecular* interactions, since those arising from *intermolecular* interactions are expected to have four times lower peak intensities. Unambiguous long-range correlations such as between Q79CD and I88CD1 were used as important tertiary structure restraints (Supplementary Fig. 17).

Finally, a ¹⁵N-dephased, ¹³C-detected frequency-selective REDOR (FS-REDOR) experiment²¹ performed on the uCN sample was used to observe the presence of salt bridge(s) between the Lys amine NZs and the Glu carboxylate CDs (Supplementary Fig. 18). As an internal control, the selective pulse on the ¹³C channel was set to encompass both the Glu CDs and the carbonyl peak. With 1.8 ms REDOR mixing, an effect is not observed for either the Glu CDs or the carbonyls. However, with 9.0 ms REDOR mixing, a 30% dephasing is observed for the Glu CD peak, but not for the carbonyls (red spectrum), confirming that at least one (and likely multiple) salt bridge(s) must be present in the fibril structure.

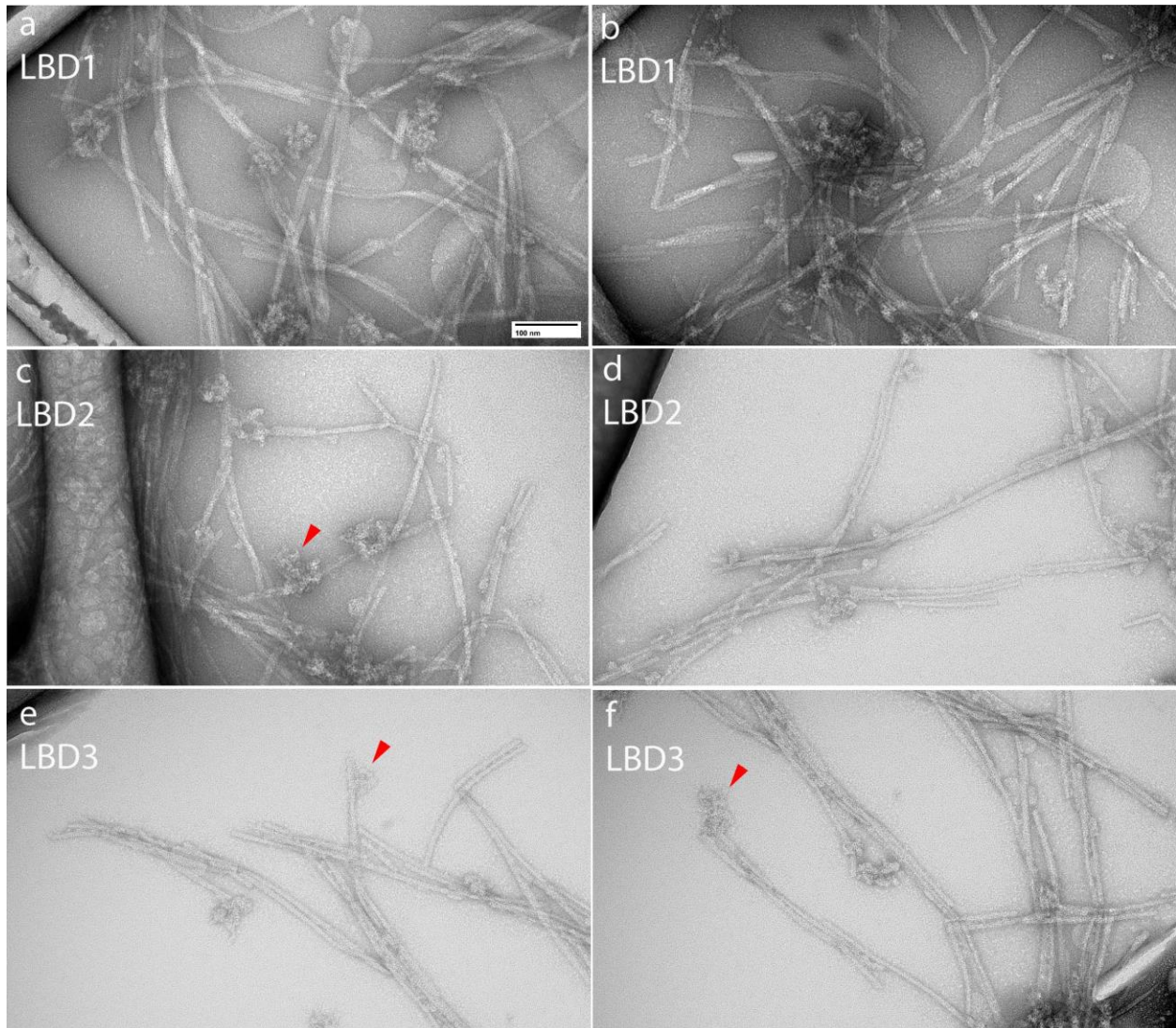
Supplementary Notes 2: SSNMR structural model demonstrates high stability in an unrestrained molecular dynamics simulation

We next proceeded to analyze the thermodynamic stability of the SSNMR structure using an unrestrained molecular dynamics (MD) simulation. While the results of this simulation do not directly validate the accuracy of the model, they demonstrate clearly that the fibril is remarkably stable (Supplementary Fig. 20a-b), and regions where NMR data is sparse correlate to regions displaying a high degree of disordering throughout the simulation. The fibril core (residues 35 to 44 and 65 to 99) show an RMSD of ~3.6 Å and an average over the whole structure of ~5.75 Å, where the higher RMSD is contributed by the disorder of the N- and C- termini and the disordered

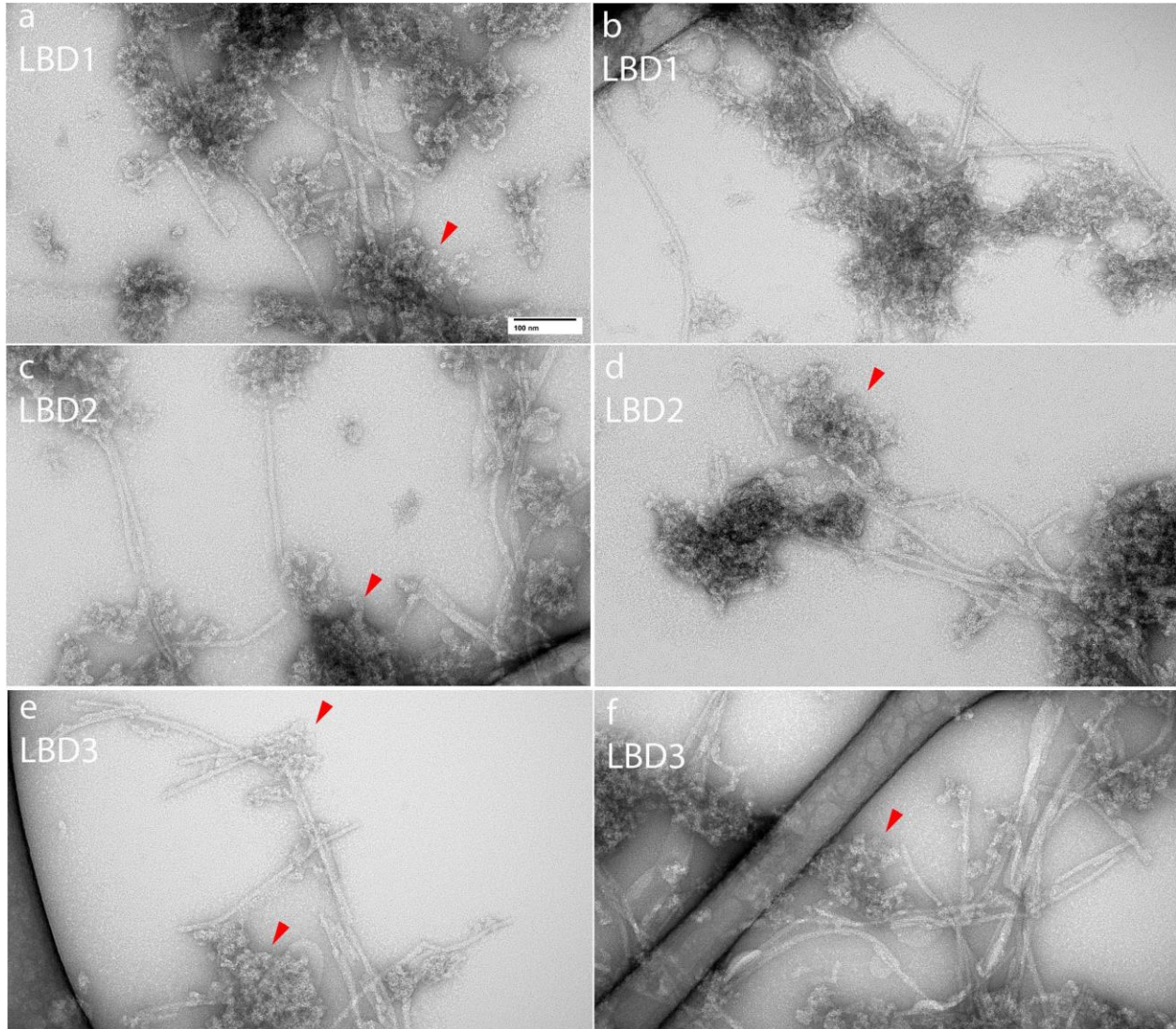
residues 45 to 64. The RMSF measured for each residue was less than 1 Å for the fibril core (Supplementary Fig. 20c) relative to the final NMR structure. After 200 ns of production MD, the overall fold remains qualitatively unchanged, however the fibril does inherit a twist (Supplementary Fig. 20d-e). The RMSD value for individual protomers relative to the SSNMR model stabilizes at about 2.5 Å, in close agreement with the uncertainty in the SSNMR bundle. The RMSD calculated for the full fibril stabilizes at about 3.25 Å, but the inflation is primarily due to the twist. Additionally, we identified ions in the simulation coordinated to specific regions within the simulation. Supplementary Fig. 20f. shows a projection along the long axis of the fibril where the ion distribution of sodium coordinate to the C-terminus and to E83. Supplementary Fig. 20g shows chloride ions coordinating predominantly to residues 32 to 45, where two KTK repeats are present within the structure, with the lysine sidechains coordinating to the chloride ion mass. This is interesting as in the cryo-EM structure of LBD fibrils display a non-proteinaceous density at this same site.



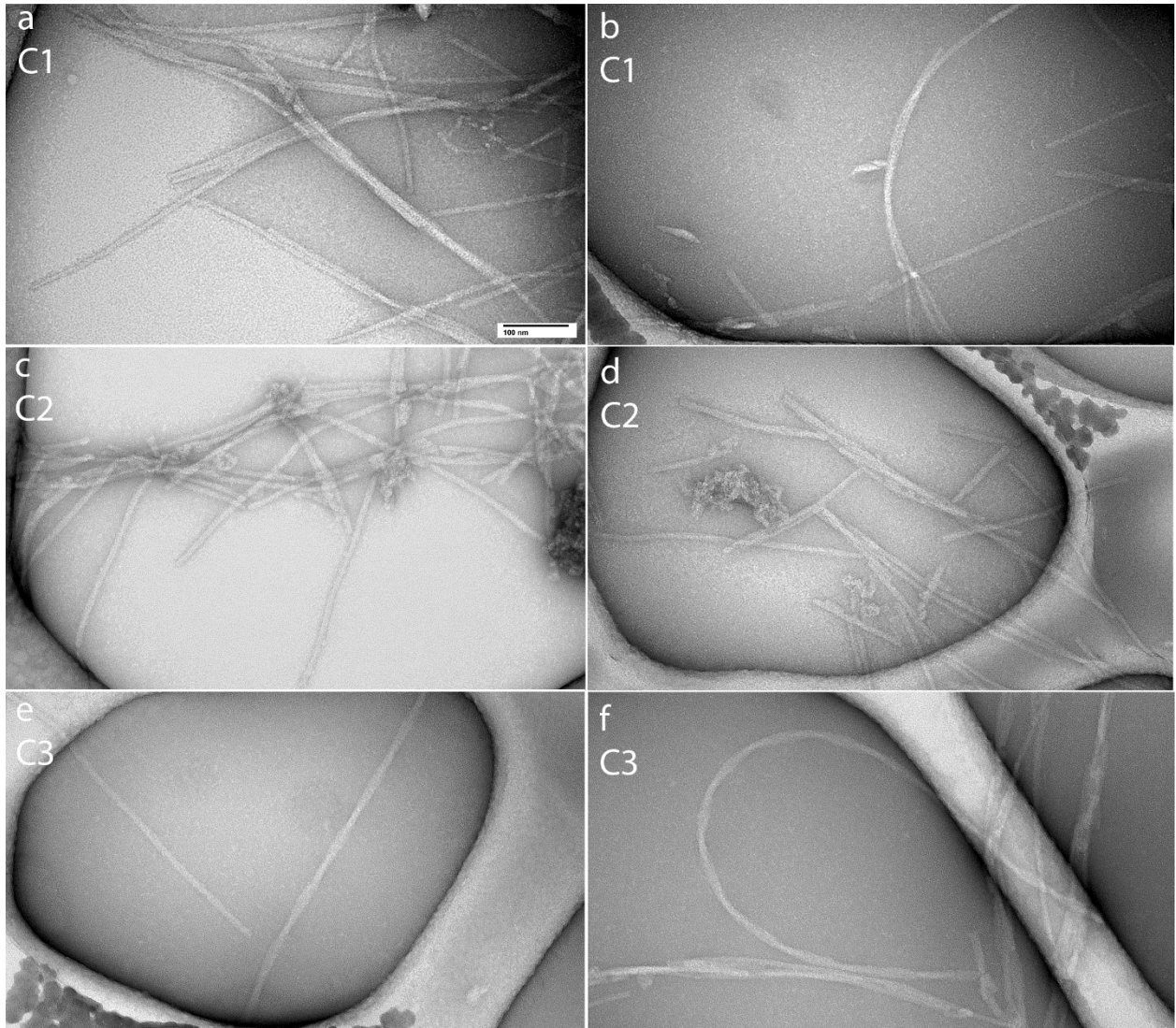
Supplementary Fig. 1: Representative negative stain TEM images of LBD amplified fibrils obtained after 6 cycles of amplification with natural abundance monomer. **a, b** LBD1. **c, d** LBD2. **e, f** LBD3. A minimum of 10 micrographs were collected for each sample. Similar results were obtained from at least three independently prepared fibril samples. Scale bar = 100 nm.



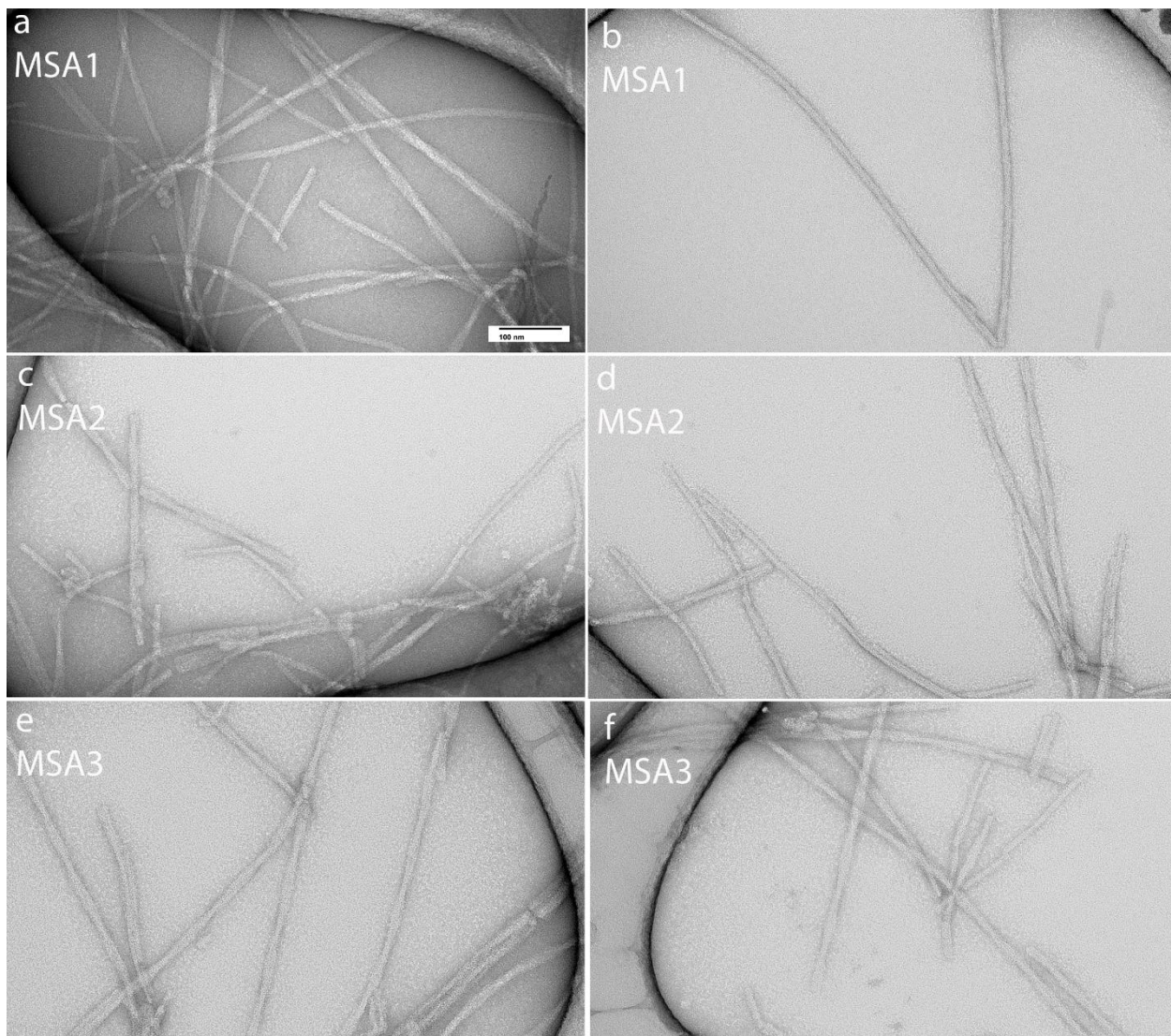
Supplementary Fig. 2: Representative negative stain TEM images of LBD amplified fibrils obtained after 4 cycles of amplification with natural abundance monomer. **a, b** LBD1. **c, d** LBD2. **e, f** LBD3. Examples of amorphous tissue-derived material from postmortem tissue insoluble fraction are indicated with red arrowheads. A minimum of 10 micrographs were collected for each sample. Similar results were obtained from at least three independently prepared fibril samples. Scale bar = 100 nM.



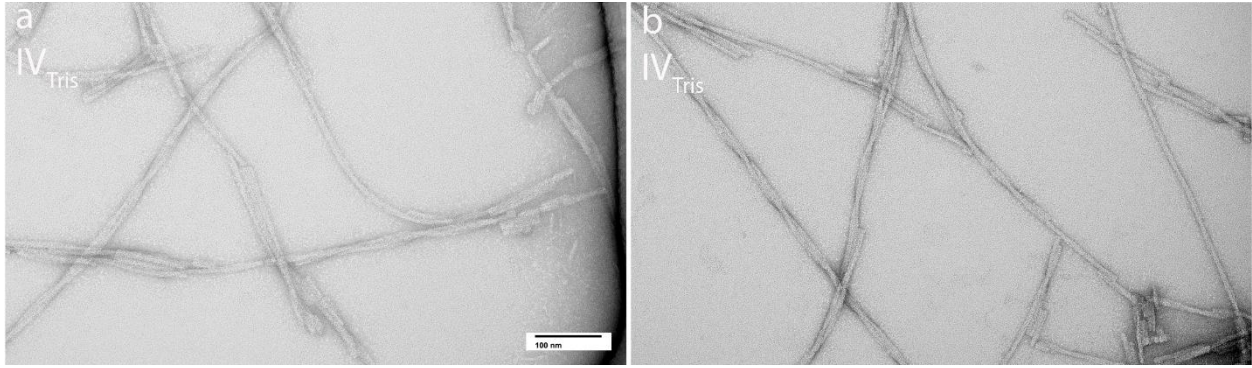
Supplementary Fig. 3: Representative negative stain TEM images of LBD amplified fibrils obtained after 2 cycles of amplification with natural abundance monomer. **a, b** LBD1. **c, d** LBD2. **e, f**, LBD3. Examples of amorphous tissue-derived material from postmortem tissue insoluble fraction are indicated with red arrowheads. A minimum of 10 micrographs were collected for each sample. Similar results were obtained from at least three independently prepared fibril samples. Scale bar = 100 nM.



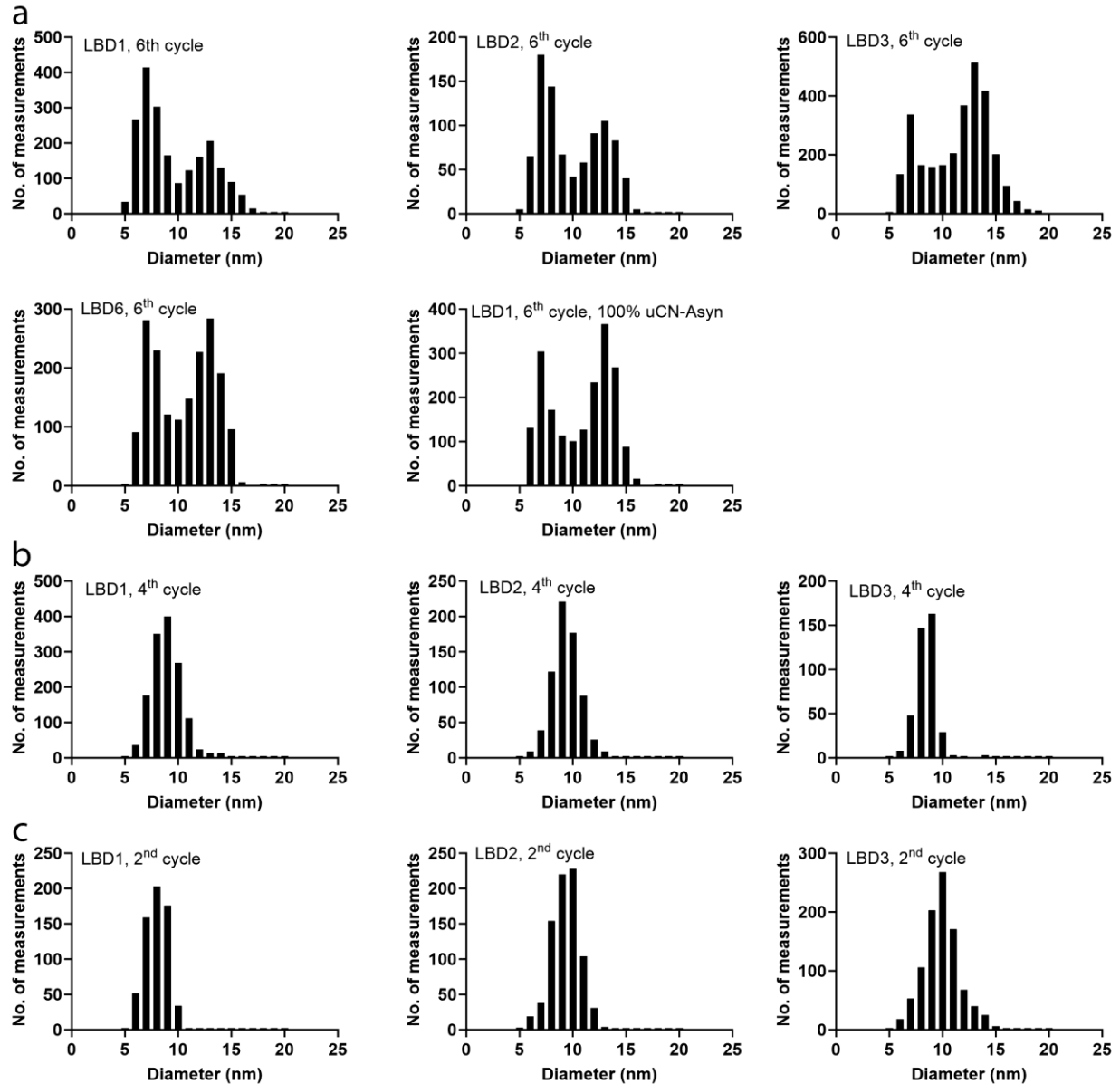
Supplementary Fig. 4: Representative negative stain TEM images of control amplified fibrils obtained after 6 cycles of amplification with natural abundance monomer. **a, b,** C1. **c, d,** C2. **e, f,** C3. A minimum of 10 micrographs were collected for each sample. Similar results were obtained from at least three independently prepared fibril samples. Scale bar = 100 nm.



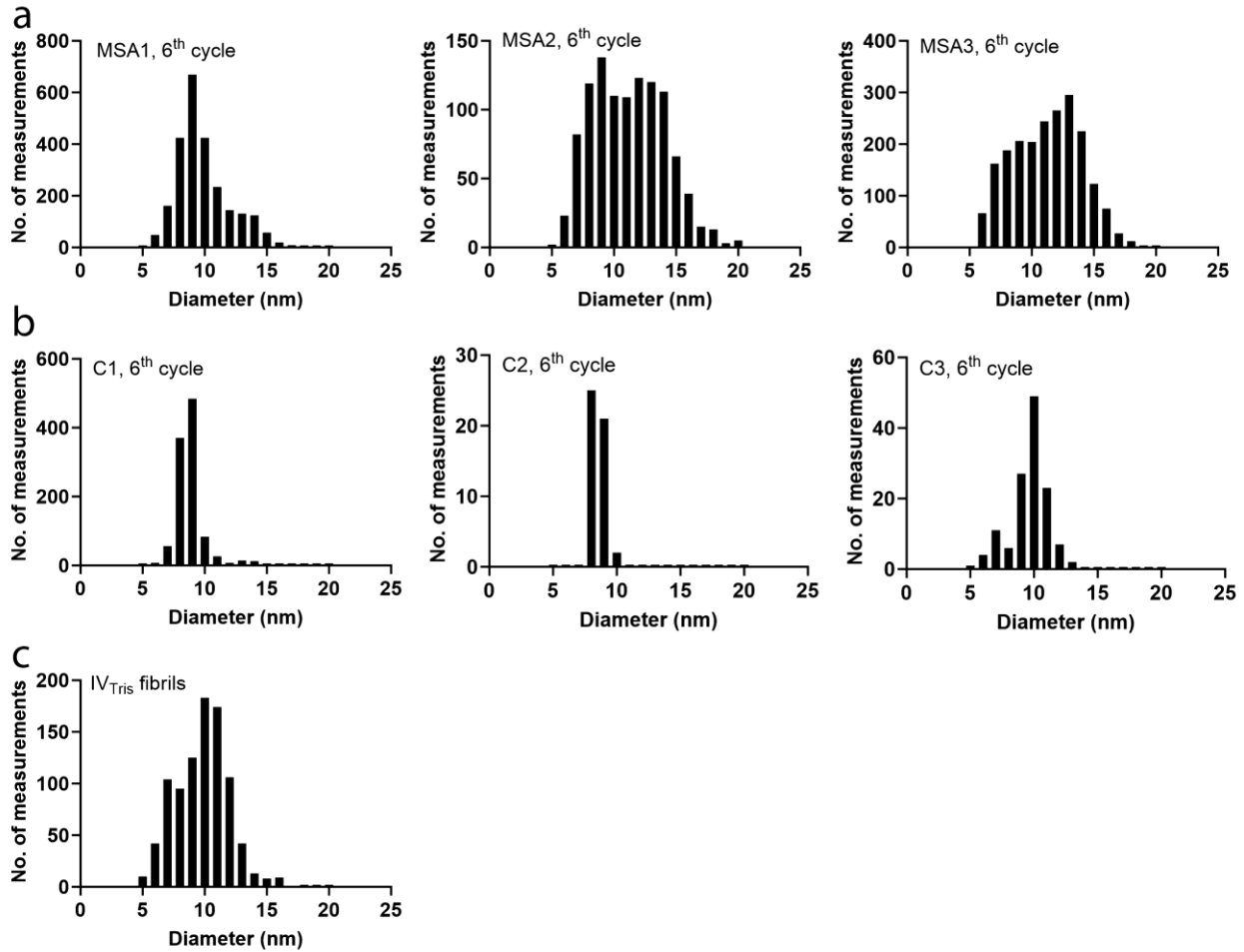
Supplementary Fig. 5: Representative negative stain TEM images of MSA amplified fibrils obtained after 6 cycles of amplification with natural abundance monomer. **a, b** MSA1. **c, d** MSA2. **e, f** MSA3. A minimum of 10 micrographs were collected for each sample. Similar results were obtained from at least three independently prepared fibril samples. Scale bar = 100 nM.



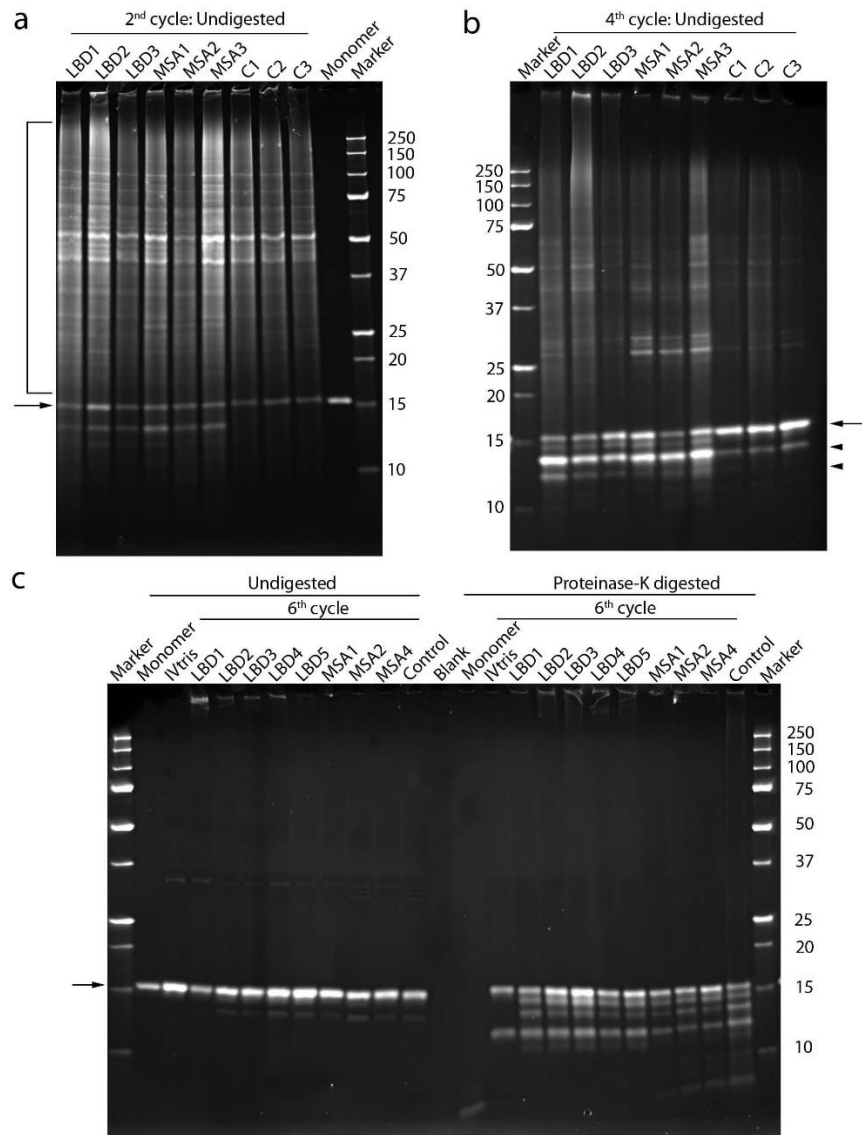
Supplementary Fig. 6: a, b Representative negative stain TEM images of in-vitro fibrils prepared in 20 mM Tris-HCl, pH 8.0 plus 100 mM NaCl buffer by nucleation (IV_{Tris}) with natural abundance monomer. A minimum of 10 micrographs were collected for each sample. Similar results were obtained from at least three independently prepared fibril samples. Scale bar = 100 nM.



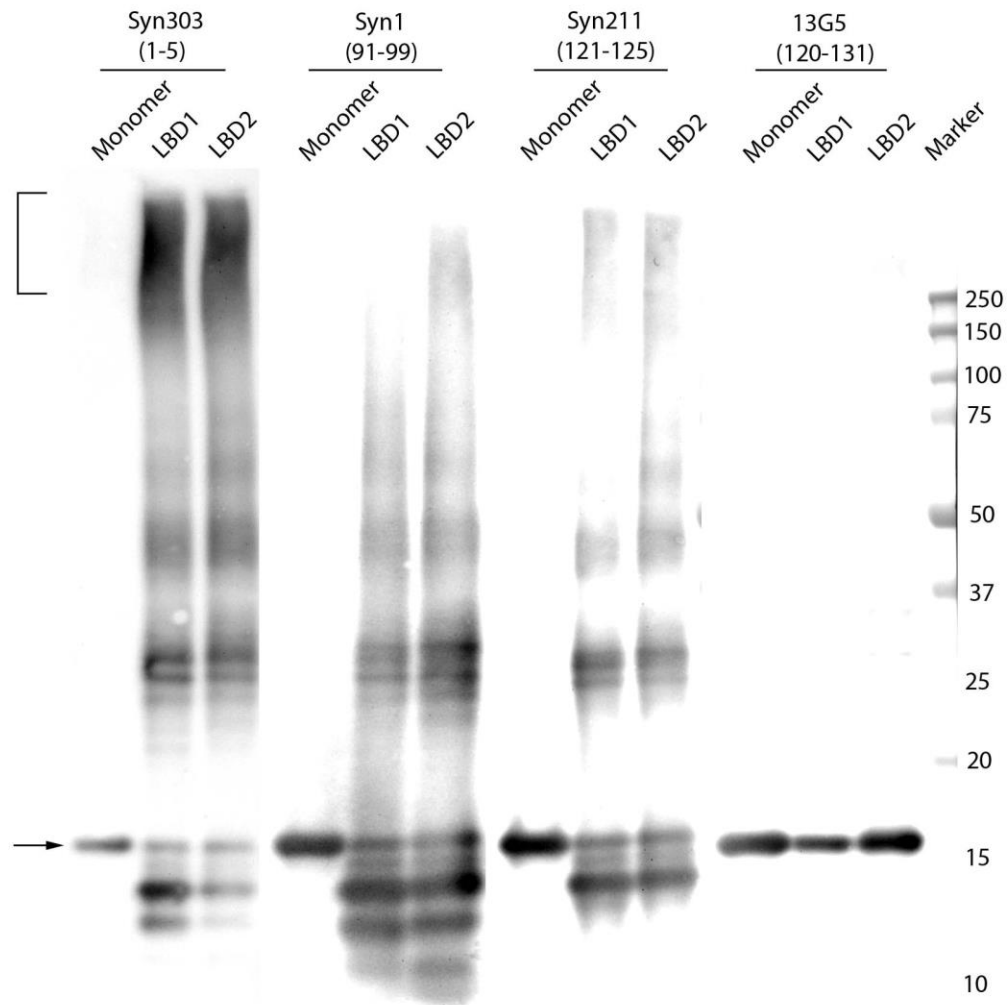
Supplementary Fig. 7: a, b, c Histograms showing distribution of diameter measurements quantified in multiple TEM images for (a) Five samples of LBD amplified fibrils after 6 cycles, (b) Three cases of LBD amplified fibrils after 4 cycles, (c) Three cases of LBD amplified fibrils after 2 cycles. A minimum of 10 micrographs were analyzed for diameter measurements for each sample. Fibril diameters have a bimodal distribution after 6 cycles of amplification, with diameters ranging from 6 nm to 15 nm, suggesting two populations with overlapping diameter measurements. A bimodal distribution is not apparent for fibrils obtained after 2 cycles or 4 cycles, which have a smaller mean diameter. Variability in diameter measurements is likely related to limited precision of measurements on negative stain TEM images and the variable rotational orientation of fibrils on the grid surface.



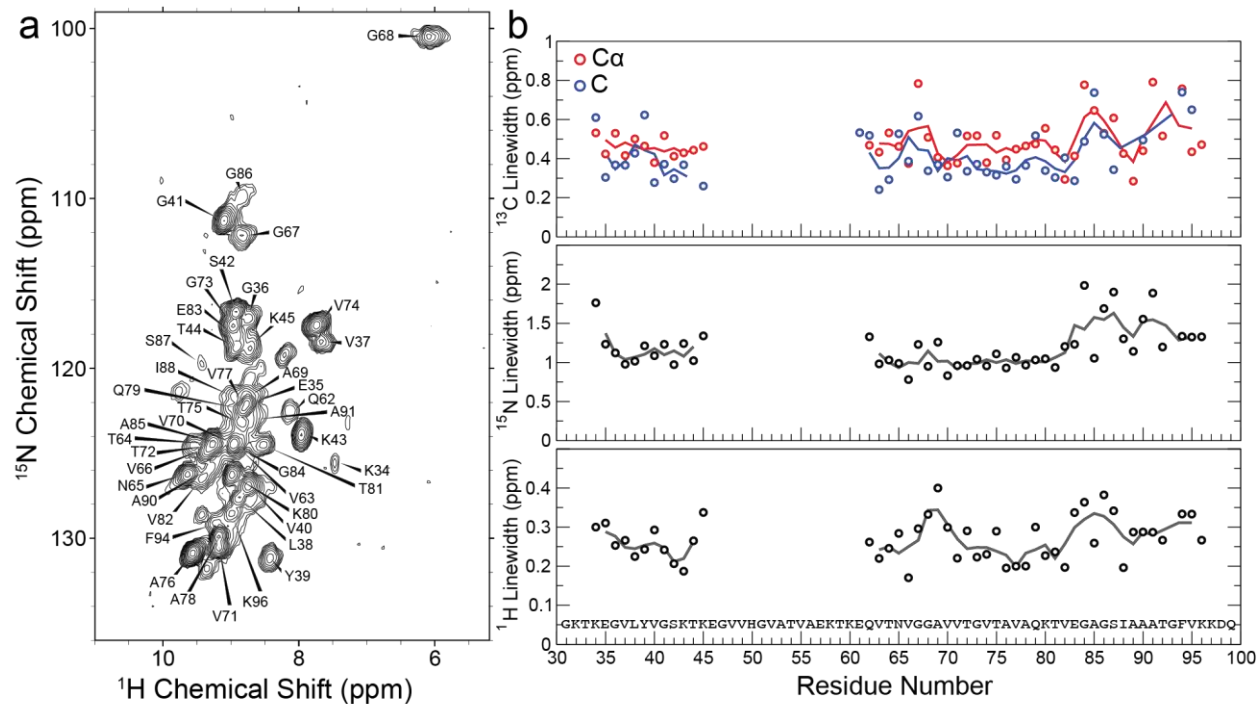
Supplementary Fig. 8: a, b, c Histograms showing quantification of diameter measurements obtained from multiple TEM images for (a) Three cases of MSA amplified fibrils after 6 cycles, (b) Three cases of control amplified fibrils after 6 cycles, (c) IV_{Tris} fibrils. A minimum of 10 micrographs were analyzed for diameter measurements for each sample.



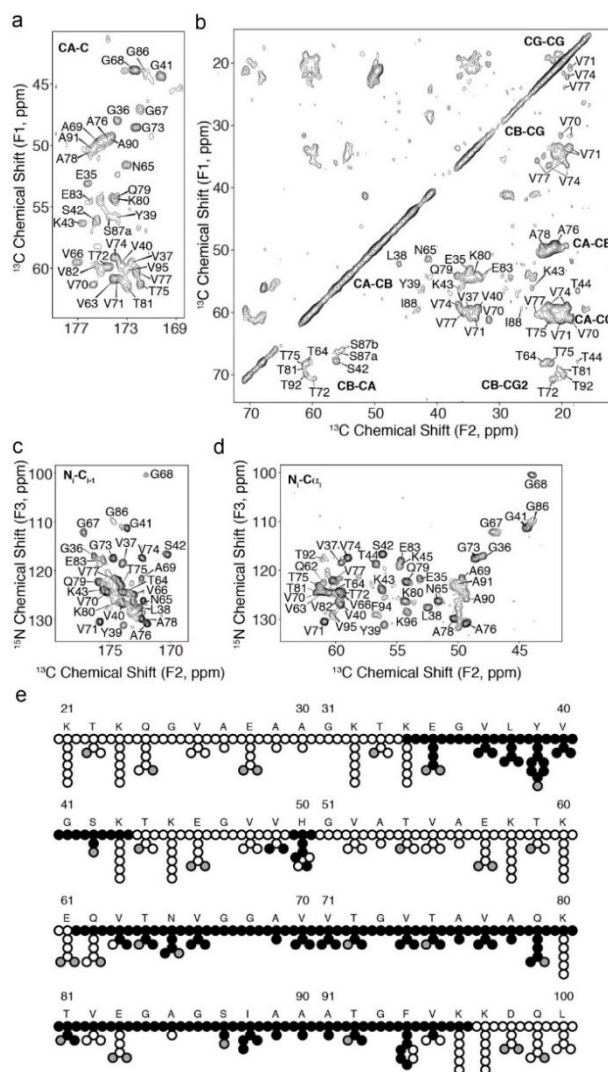
Supplementary Fig. 9: SDS-PAGE gel electrophoresis of amplified fibrils. Equal amounts of IV_{Tris}, LBD amplified, MSA amplified and Control amplified fibrils were treated with 2% SDS and run on a 12% Bis-Tris gel. SYPRO Ruby protein gel stain was used to visualize the proteins. **a** SDS-PAGE of three cases of LBD, MSA, and Control amplified fibrils after 2 cycles. Purified recombinant monomeric Asyn (Monomer) was included for comparison. **b** SDS-PAGE of three cases of LBD, MSA, and Control amplified fibrils after 4 cycles. **c** SDS-PAGE of undigested and Proteinase-K digested LBD (5 cases), MSA (4 cases,) and control (pooled from 3 cases) amplified fibrils after 6 cycles. All samples were amplified with natural abundance WT Asyn monomer. The black arrow indicates a full-length Asyn monomer. Additional tissue-derived proteins (indicated by brackets) are abundant after the 2nd cycle and are decreased relative to Asyn after 4th and 6th cycles. A high percentage of Asyn cleavage products (arrowheads) at approximately 12-14 kD are present after the 2nd and 4th cycles and are decreased relative to full length Asyn after the 6th cycle. Similar results were obtained from two independent experiments.



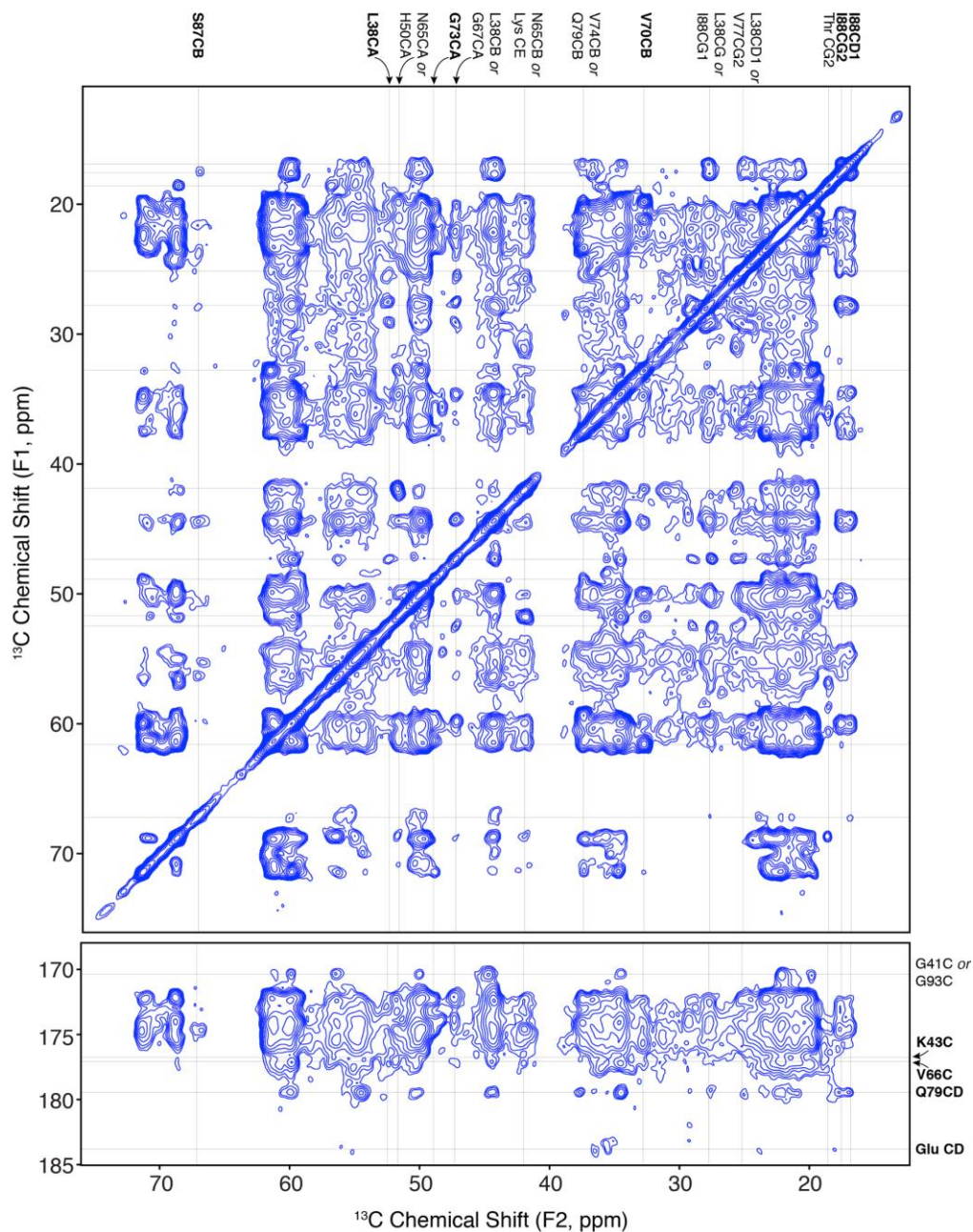
Supplementary Fig. 10: Western blot analysis of LBD amplified fibril samples using anti-Asyn antibodies that recognize a range of epitopes in Asyn protein. Western blot of 4th cycle LBD amplified fibrils with antibodies Syn303 (epitope: amino acids (aa) 1-5)²², Syn1 (epitope: aa 91-99), Syn211 (epitope: aa 121-125) and 13G5 (epitope: aa 120-131) indicate that the cleavage products lack C-terminal epitopes but not N-terminal epitopes. This C-terminal cleavage of Asyn that occurs during fibril amplification corresponds to a high percentage of C-terminal cleavages present in Asyn fibrils extracted from human brain tissue²³⁻²⁵. Several antibodies also recognize higher molecular weight Asyn species that are likely multimeric forms, particularly Syn303 which is derived from immunization with oxidized and aggregated Asyn and preferentially immunostains pathologic Asyn (bracket)²⁶. Purified full-length recombinant monomeric Asyn (Monomer) is included for comparison (black arrow). n=2 for LBD amplified fibril samples, experiment was performed once.



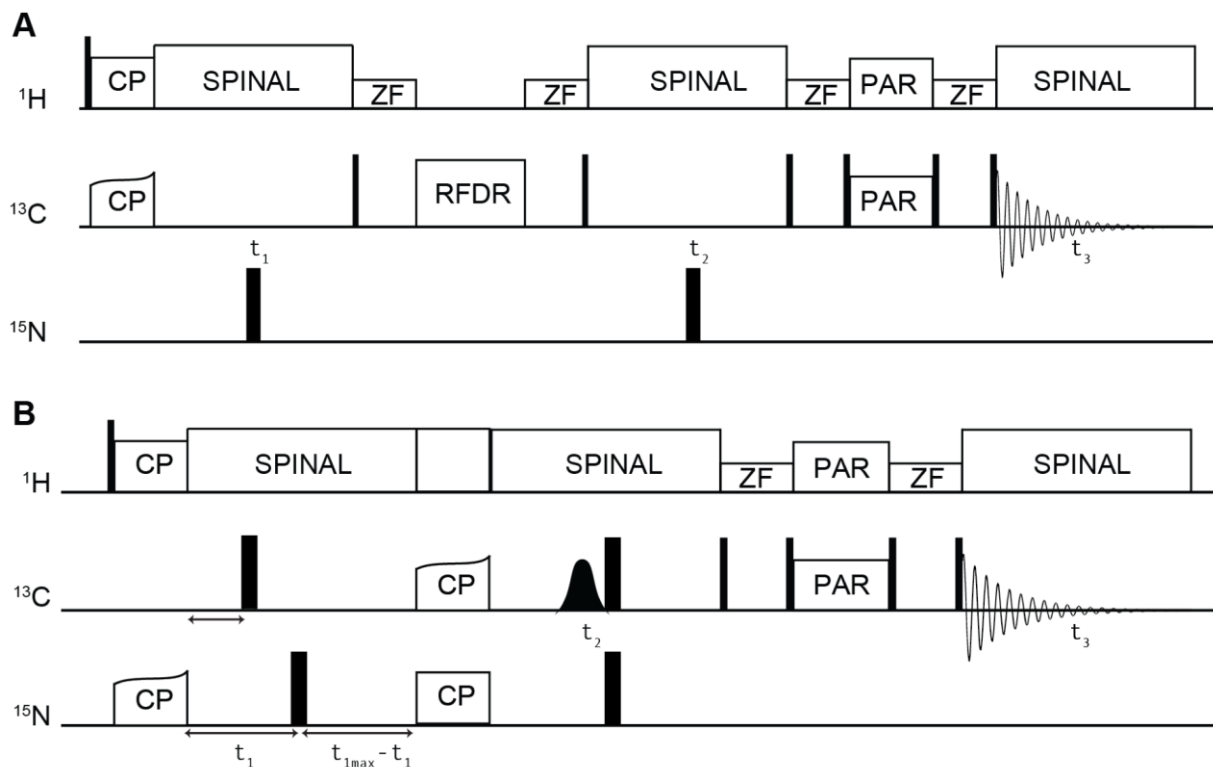
Supplementary Fig. 11: **a** ^1H - ^{15}N projection of 3D hCANH spectrum. **b** ^{13}C (top), ^{15}N , and ^1H (bottom) linewidths of assigned residues of the ^{13}C , ^2H , ^{15}N sample. Three residue moving average is shown as a solid line through plot. Source data are provided as a Source Data file.



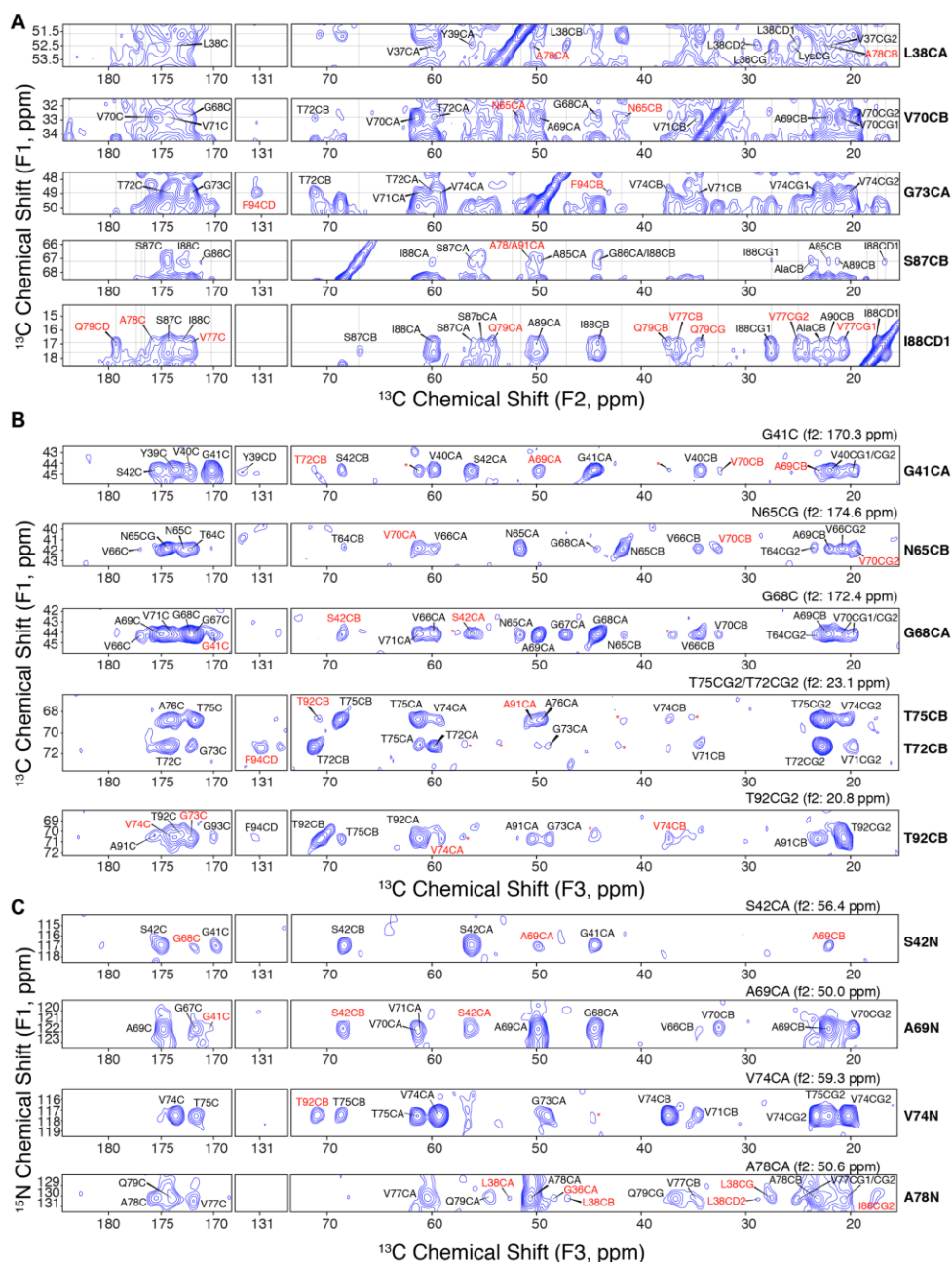
Supplementary Fig. 12: Two-dimensional SSNMR spectra collected on uniformly ^2H , ^{13}C , ^{15}N -labeled LBD Asyn fibril. **a** ^{13}C - ^{13}C spectrum showing alpha to carbonyl correlations. Data was acquired at 750 MHz ^1H frequency with 33.333 kHz magic-angle spinning and sample temperature 10 ± 5 $^\circ\text{C}$ with 9 ms CTUC-COSY mixing. The indirect dimension was extended two-fold during processing using SMILE. **b** ^{13}C - ^{13}C spectrum showing aliphatic correlations. Data was acquired at 500 MHz ^1H frequency with 22.222 kHz magic angle spinning and a variable temperature set point of 0 $^\circ\text{C}$ with 11.8 ms fpRFDR mixing. **c** ^{15}N - ^{13}C projection from a 3D CONH experiment showing backbone correlations between amide nitrogens and carbonyl carbons. **d** ^{15}N - ^{13}C projection from a 3D CANH spectrum showing backbone correlations between amide nitrogens and alpha carbons. Data in **(b)** and **(c)** were acquired at 750 MHz ^1H frequency with 33.333 kHz magic-angle spinning and sample temperature 10 ± 5 $^\circ\text{C}$, using a 6 ms ^{15}N - ^{13}C cross polarization. 3Ds were collected using non-uniform sampling followed by reconstruction using SMILE prior to Fourier transformation. **e** Assigned atoms showing residues K21 to L100 out of 140 total amino acids in the Asyn primary sequence. Atoms with assignments are represented as filled black circles, filled gray circles are oxygen, and empty circles are unassigned or left empty due to uncertainty in the assignment.



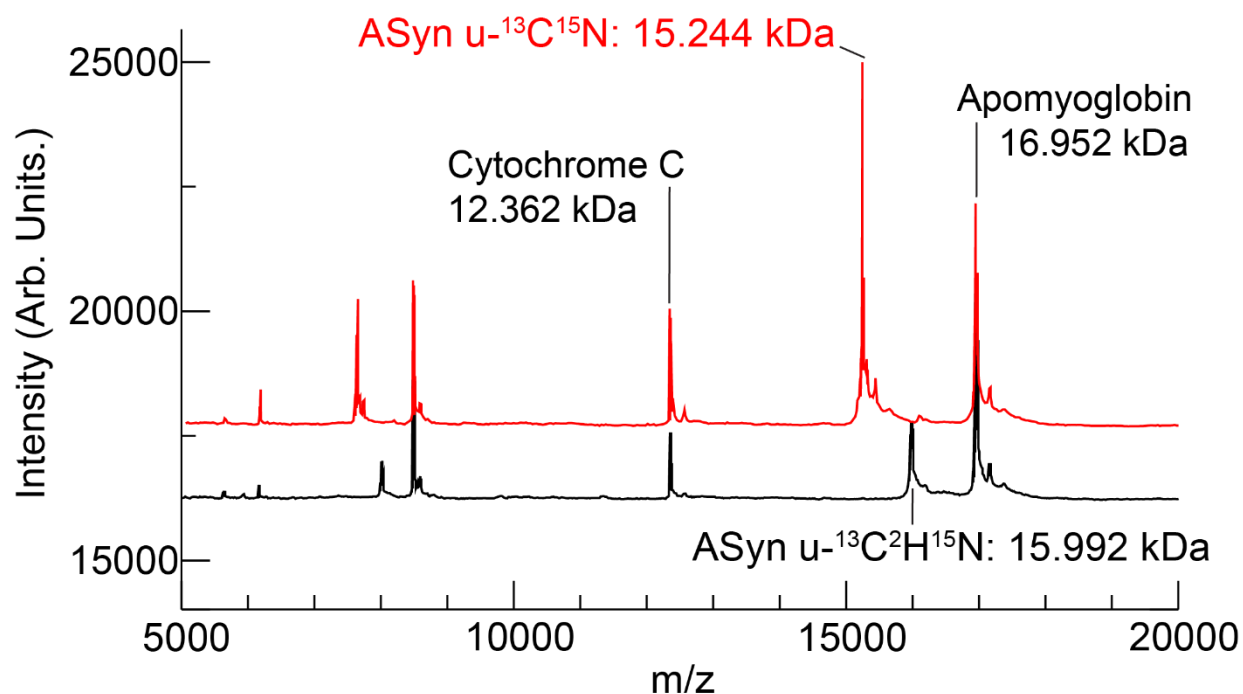
Supplementary Fig. 13: Two-dimensional ^{13}C - ^{13}C correlation spectrum acquired with PAR mixing on uniformly ^{13}C , ^{15}N -labeled LBD Asyn fibril. ^{13}C - ^{13}C correlation spectrum showing the aliphatic-aliphatic (top panel) and aliphatic-carbonyl (bottom panel) regions. Data was acquired at 750 MHz ^1H frequency with 16.667 kHz magic-angle spinning with 12 ms PAR mixing. The first contour is cut at 6 times the root-mean-square noise. Horizontal and vertical lines are drawn to indicate all strips with one of the two assignments being either unambiguous (Bold atom labels) or two-fold ambiguous (regular text labels).



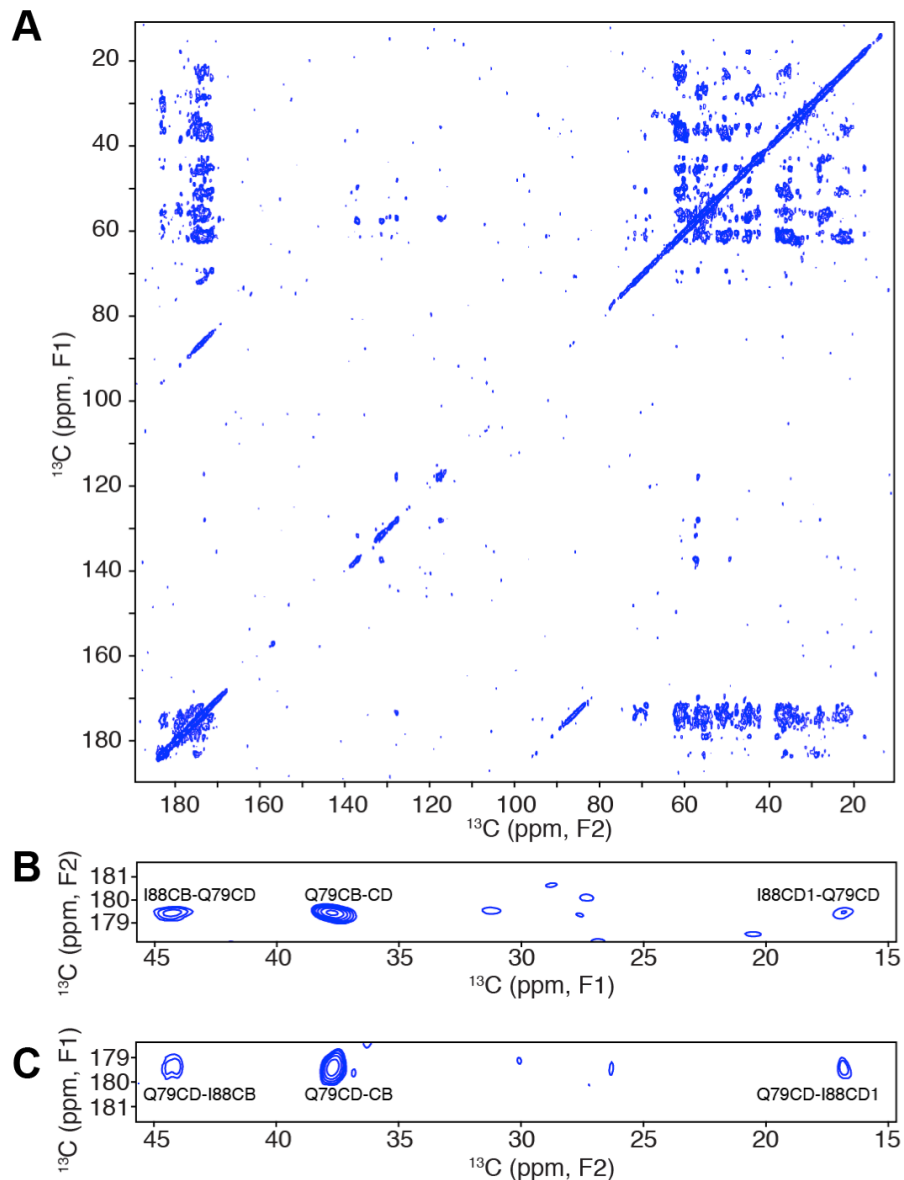
Supplementary Fig. 14: Pulse sequence diagrams for 3D experiments with PAR mixing. **a** Pulse sequence used to collect broadband ^{13}C - ^{13}C - ^{13}C correlation spectrum. **b** Pulse sequence used to collect ^{15}N - $^{13}\text{C}\alpha$ - $^{13}\text{C}\alpha$ correlation spectrum utilizing constant-time evolution for ^{15}N and a J-decoupling soft pulse for $^{13}\text{C}\alpha$. Both experiments can be done using non-uniform sampling of the two indirect dimensions.



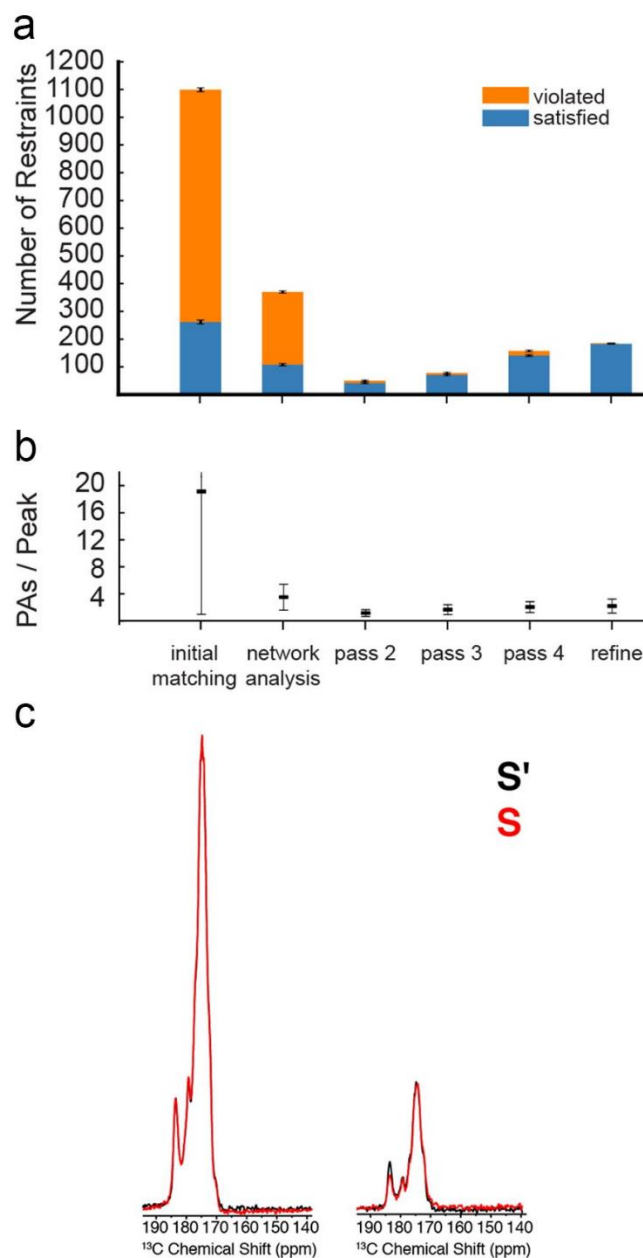
Supplementary Fig. 15: Long-range correlations detected in 2D and 3D PAR experiments. **a** Strip plots with assignment labels from the spectrum in Extended Data Fig. 5 showing correlations from five atoms with unique assignments in F1. **b** 2D strip plots from a 3D ^{13}C - ^{13}C - ^{13}C correlation spectrum showing correlations from six residues that are disambiguated in F1 and F2 relative to the 2D spectrum. **c** 2D strip plots from a 3D ^{15}N - $^{13}\text{C}\alpha$ - $^{13}\text{C}\chi$ correlation spectrum showing correlations from four residues with unique ^{15}N - $^{13}\text{C}\alpha$ shifts. All direct-dimension assignments are unique, arising from nearest neighbor residues or based on a network analysis. Long-range assignments are shown in red. Red asterisks indicate peaks that cannot be assigned based on the resonance list, cannot be disambiguated based on a network analysis, or are out of plane in the 3Ds.



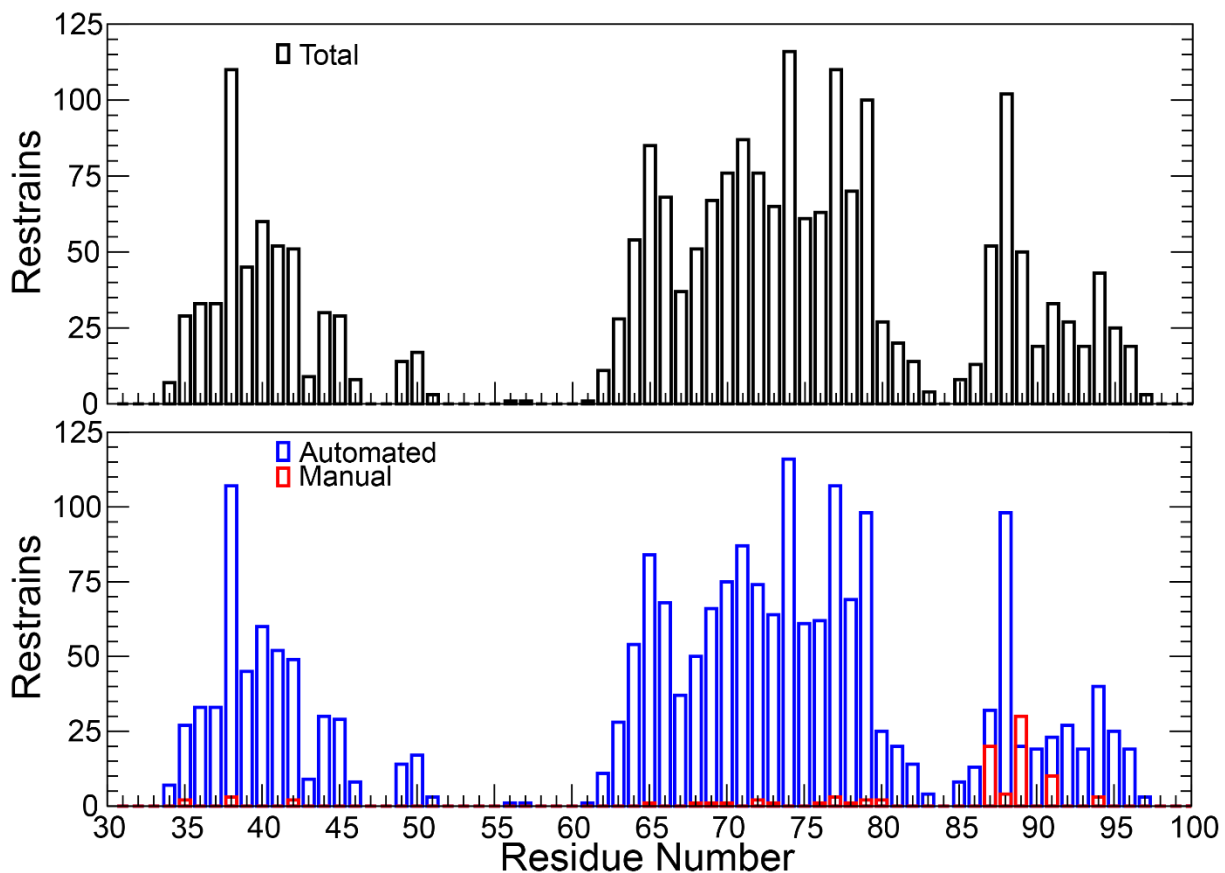
Supplementary Fig. 16: MALDI of Asyn to determine isotopic enrichment. Monoisotopic mass is 14.451 kDa at pH 4. U-¹³C-¹⁵N Asyn (red) enrichment was determined to be 99.9% ¹³C-¹⁵N incorporation (15.244kDa -14.451kDa/ 793 C and N sites in Asyn). U-¹³C-²H-¹⁵N Asyn(black) enrichment was determined to be 94.6% (15.992 – 15.244 (assuming the same ¹³C and ¹⁵N incorporation as the U-¹³C-¹⁵N growth) / 792 non-exchangeable ¹H sites in Asyn). Cytochrome C and Apomyoglobin are added as calibration standards with masses of 12.362 kDa and 16.952 kDa, respectively.



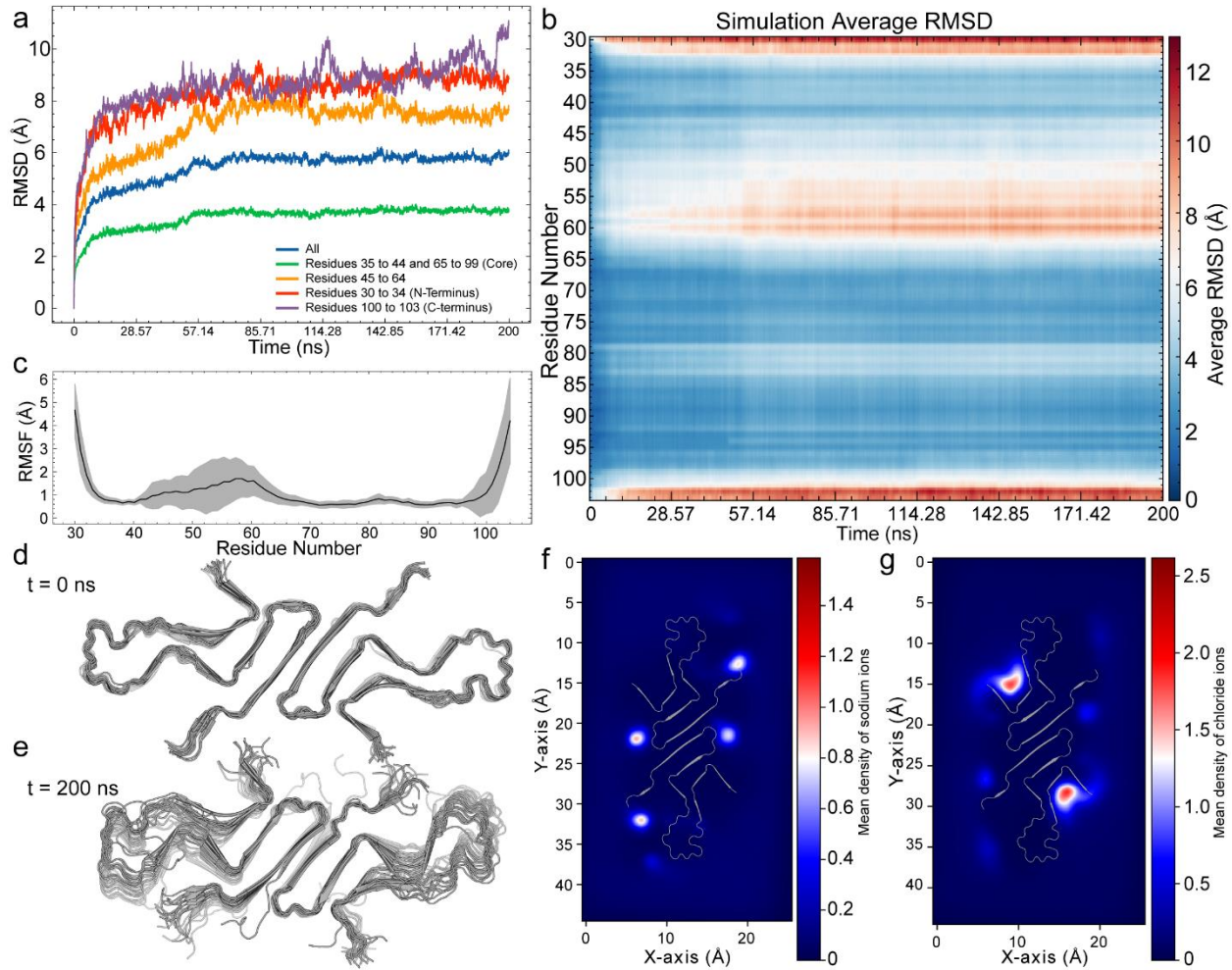
Supplementary Fig. 17: Two-dimensional ^{13}C - ^{13}C correlation spectrum acquired with DARR mixing on 25% [$2\text{-}^{13}\text{C}$]glycerol, ^{15}N 75% natural abundance LBD Asyn fibril. **a** ^{13}C - ^{13}C correlation spectrum showing the entire spectrum. **b** Inset of I88-Q79CD correlations from upper left of diagonal. **c** Inset of Q79CD-I88 correlations from lower right of diagonal. Data was acquired at 500 MHz ^1H frequency with 11.111 kHz magic-angle spinning and a variable temperature set point of 0 $^\circ\text{C}$ with 500 ms DARR mixing. The first contour is drawn at 5 times the root-mean-square noise.



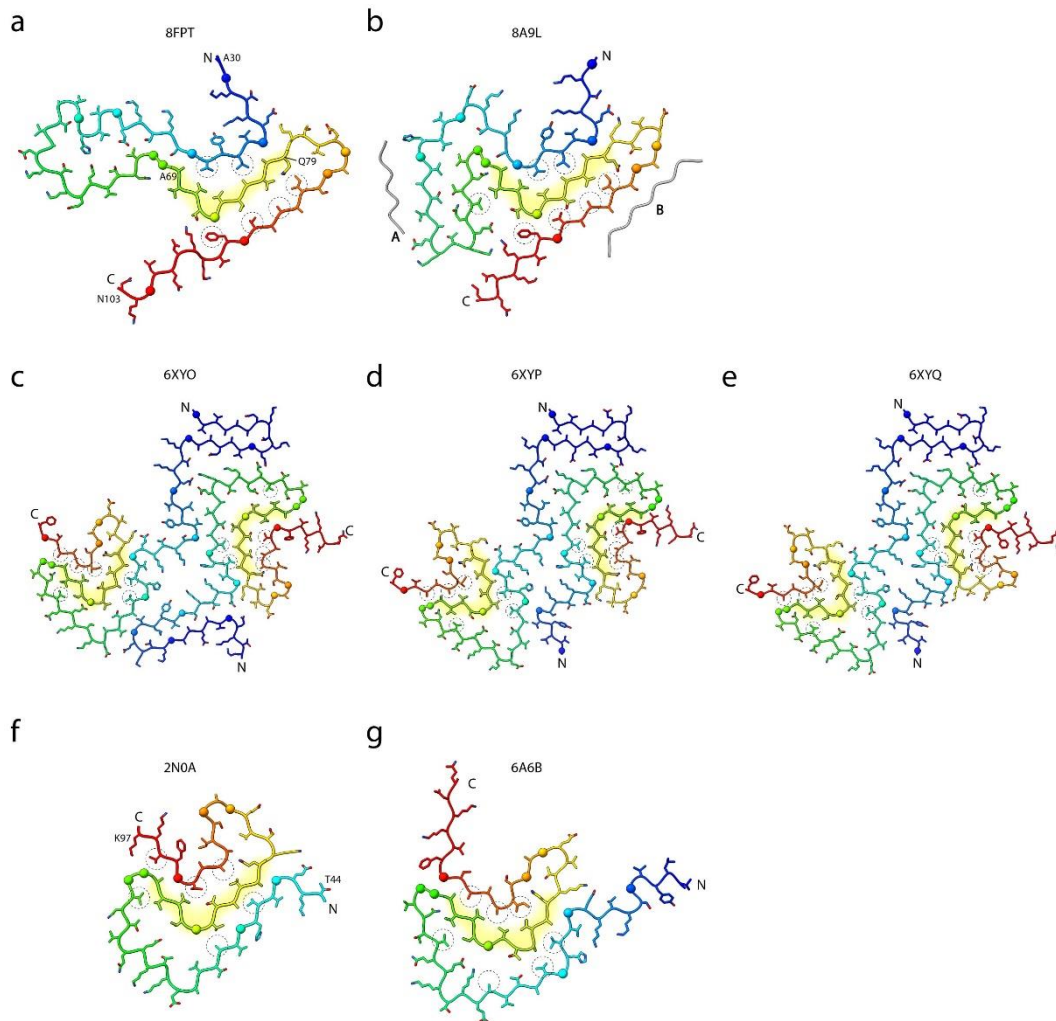
Supplementary Fig. 18: PASD Results and FS-REDOR analysis. **a** Stacked bar chart showing the average number of restraints that are satisfied (blue) and violated (orange) by the top five lowest energy structures generated by the final refinement at each stage of the PASD structure calculation and refinement protocol. **b** Average number of peak assignments (PAs) per peak at each stage of PASD. A high-likelihood cutoff of 0.90 was used. Error bars represent ± 1 standard deviation ($n=11$). **c** Detection of salt bridges by FS-REDOR. ^{15}N -dephased, ^{13}C -detected frequency-selective REDOR (FS-REDOR) performed on uniformly ^{13}C , ^{15}N -labeled LBD Asyn fibril. Gaussian pi pulses were used to selectively reintroduce the dipolar couplings between the Lys NZ and the Glu CD resonances. The reference spectrum (S') is plotted in black and the REDOR dephased spectrum is in red (S) for short mixing (1.8 ms) and moderate mixing (9.0 ms).



Supplementary Fig. 19: Distance restraints used for structure calculation. Top: Total Restrains used for the structure calculation presented in main text. Bottom: Automated and Manual restraints used for structure calculation. The restraints shown here correspond to their respective lines drawn in Figure 6c. Source data are provided as a Source Data file.



Supplementary Fig. 20: Unrestrained MD simulation (200 ns) of LBD fibril (2x 20-mer) from residues 30 to 103. Protomers corresponding to the top two and the bottom two protofilaments were removed as they do not replicate the extended nature of the fibril. **a** RMSD of the full simulation time shown for all residues and specific portions of the structure. **b** Residue specific RMSD averaged over each residue, $n=36$. **c** Residue specific RMSF of the fibril of the last 193 ns of the simulation, corresponding to where the RMSD in A and B plateau. **d-e** Initial and final frames, respectively, of the simulation looking down the long axis of the fibril. **f** Mean density distribution of sodium ions within the simulation, with four major sites arranged symmetrically across the protomers, coordinating to E83 and the C-terminus. **g** Mean density distribution of chloride ions with a major coordination site between the lysines at residue 32, 34, 43, and 45, which are all pointing in towards the chloride ion density. This suggests that ions act as stabilizing forces regions of the fibril where charged residues stacked along the fibril axis and are not involved in salt bridge formation, neutralizing the charges present along the surface exposed residues along the long axis of the fibril.



Supplementary Fig. 21: The conserved L-shaped motif in Asyn models. The L-shaped motif is comprised of residues 69-79 (highlighted in yellow) in the hydrophobic core of LBD amplified (a) and LBD extracted (b), MSA (c-e), and in vitro (f-g) Asyn fibrils. All models are colored by Jones' rainbow from N-terminus (blue) to C-terminus (red). Hydrophobic residues that interact with the L-motif are circled by a dotted line. The α -carbons of all glycine residues are depicted as a large sphere, and the unidentified proteinaceous islands 'A' and 'B' in the cryo-EM Asyn model (b) are in grey. Notably, the side chains pointing inside of the L-motif (A69, V71, etc.) interact with N-terminal strands (residues 35-42) in LBD structures, whereas they interact with C-terminal strands in MSA and in vitro structures (residues 86-94). Inversely, the side chains facing out of the L-motif interact with C-terminal strands (residues 86-97) in the LBD structures and with N-terminal strands in the MSA and in vitro structures (residues 41-66). The ability of Asyn to retain this embedded L-shape motif amongst such heterogeneity in folds is likely due to the high number of glycine residues.

Supplementary Table 1: Concentration of amplified fibrils produced with natural abundance monomer, as determined by the [³H]-BF2846 radioligand binding assay. Fold amplification represents the ratio of the concentration for each LBD sample to the mean concentration for the Control samples. Source data are provided as a Source Data file.

Case	After 6 cycles	
	Concentration (μM)	Fold amplification
LBD1	92.6	17.1
LBD2	94.2	17.4
LBD3	87.3	16.1
LBD4	189.3	34.9
C1	4.0	
C2	10.1	
C3	2.2	

Supplementary Table 2: Concentration of amplified fibrils produced with isotopically labeled Asyn monomer (uCN-Asyn), as determined by the [³H]-BF2846 radioligand binding assay. Source data are provided as a Source Data file.

Case	After 4 cycles		After 6 cycles	
	Concentration (μM)	Fold amplification	Concentration (μM)	Fold amplification
LBD1	39.83	22.8	42.24	11.5
LBD2	19.65	11.2		
C1	2.88		3.15	
C2	0.62		4.19	

Supplementary Table 3: Concentration of amplified fibrils produced with isotopically labeled Asyn monomer (CDN-Asyn), as determined by the [³H]-BF2846 radioligand binding assay. Source data are provided as a Source Data file.

Case	After 4 cycles		After 6 cycles	
	Concentration (μM)	Fold amplification	Concentration (μM)	Fold amplification
LBD1	20.19	30.9	29.12	19.3
LBD2	12.50	19.1		
C1	0.99		0.26	
C2	0.31		2.76	

Supplementary Table 4: Concentration of amplified fibrils produced with uCN and CDN isotopically labeled monomer, as determined by the micro-BCA assay. 10 tubes of LBD1 uCN-Asyn and 11 tubes of LBD1 CDN-Asyn amplified fibrils were pooled together and a pooled sample taken for the micro-BCA assay.

Case	Asyn Monomer	After 6 cycles	
		Fibril concentration (μM)	Total yield (μg)
LBD1	uCN-Asyn	43.4 (average of 10 tubes)	5035
C1	uCN-Asyn	6.4	73.4
C2	uCN-Asyn	5	58
LBD1	CDN-Asyn	33.4 (average of 11 tubes)	4197.6
C1	CDN-Asyn	2.2	25.1
C2	CDN-Asyn	2.3	26.5

Supplementary Table 5: Comparison of radioligand binding vs. A_{280} assays for measuring LBD amplified fibril concentration after 6 cycles. The average inter-assay % CV was 7.6. Source data are provided as a Source Data file.

Sample	Concentration (μM), Radioligand assay	Concentration (μM), GdnHCl- A_{280}	Inter-assay %CV
LBD1	64.7	59.5	5.9
LBD2	55.3	48.3	9.5
LBD3	56.7	63	7.4

Supplementary Table 6: Comparison of MicroBCA vs. A_{280} assays for measuring LBD amplified fibril concentration after 6 cycles. The average inter-assay %CV was 6.3. Source data are provided as a Source Data file.

Sample	Concentration (μM), MicroBCA assay	Concentration (μM), GdnHCl- A_{280}	Inter-assay %CV
LBD1	70.7	59.5	12.1
LBD2	47.6	48.3	1.0
LBD3	68.6	63	6.0

Supplementary Table 7: Quantification of inclusions formed after seeding of LBD and MSA amplified fibrils in HEK293 biosensor cells. Data represented as mean \pm S.D., n =2 independent experiments =2. Source data are provided as a Source Data file.

Case	Inclusions/pg fibrils
LBD3	2.7 \pm 0.3
LBD4	6.6 \pm 2.5
LBD5	4.6 \pm 2.1
MSA1	512.9 \pm 145
MSA2	601.9 \pm 170
MSA3	602.1 \pm 0

Supplementary Table 8: Human postmortem brain tissue cases used for the study. Grey matter from caudate (Cau) and Middle Frontal Gyrus (MFG) brain regions were selected for amplification.

Case	Sex (Male/Female)	Age at Death, median (range)	Disease Duration (years)	Post-mortem interval (hours)	Primary Diagnosis	Brain Region	Braak LB Stage (0-6)	Amyloid Stage (A-C)	BRAAK NFT Stage (I-VI)
LBD1	5/2	77 (71-82)	6	14	LBD	Cau	6	C	II
LBD2			15	4	LBD	Cau	6	0	I
LBD3			4	n/a	LBD	Cau	6	C	III
LBD4			12	14	LBD	Cau	6	A	V
LBD5			11	3	LBD	Cau	6	0	III
LBD6			17	14	LBD	MFG	6	C	III
LBD7			10	11	LBD	MFG	6	C	III
MSA1	3/1	58.5 (58-65)	4	22	MSA	Cau	0	0	I
MSA2			3	12	MSA	Cau	0	0	0
MSA3			3	7	MSA	Cau	0	0	0
MSA4			6	5	MSA	Cau	0	A	I
C1	2/1	78 (73-85)	13	30	disease-control	Cau	0	0	I
C2			8	28	disease-control	Cau	0	0	IV
C3			30	22	disease-control	Cau	0	C	III

Supplementary Table 9: Solid-state NMR experiments

Sample	Experiment	Magnet	MAS Rate (kHz)	Mixing Time (ms)	NUS sampling density (%)	Exp. Time (hr)
uCN	2D ¹³ C- ¹³ C with DARR mixing	17.6 T (WB)	16.667	75, 300, 500	N/A	2.8, 76.8, 92.0
uCN	2D ¹³ C- ¹³ C with SPC7 mixing	17.6 T (WB)	16.667	0.96	N/A	20.9
uCN	3D ¹⁵ N- ¹³ CA- ¹³ CX with DARR mixing	17.6 T (WB)	16.667	75	25	37.8
uCN	3D ¹⁵ N- ¹³ CO- ¹³ CX with DARR mixing	17.6 T (WB)	16.667	75	12.5	47.3
uCN	3D ¹³ CA- ¹⁵ N- ¹³ CO	17.6 T (WB)	16.667	N/A	N/A	90.4
uCN	2D ¹³ C- ¹³ C with DARR mixing	11.7 T (WB)	22.222	50, 200, 500	N/A	5.4, 39.9, 130.6
uCN	2D ¹⁵ N- ¹³ CA	11.7 T (WB)	22.222	N/A	N/A	4.4
uCN	2D ¹⁵ N- ¹³ CO	11.7 T (WB)	22.222	N/A	N/A	0.9
uCN	3D ¹⁵ N- ¹³ CA- ¹³ CX with DARR mixing	11.7 T (WB)	22.222	200	12.5	363
uCN	3D ¹⁵ N- ¹³ CO- ¹³ CX with DARR mixing	11.7 T (WB)	22.222	200	12.5	152
uCN	3D ¹⁵ N- ¹³ CO- ¹³ CA with SPC5 mixing	11.7 T (WB)	22.222	1.26	12.5	61.4
uCN	3D ¹³ CA- ¹⁵ N- ¹³ CO	11.7 T (WB)	22.222	N/A	12.5	41.0
uCN	2D ¹³ C- ¹³ C with PAR mixing	17.6 T (WB)	17.007	12.9	N/A	56.8
uCN	3D ¹³ C- ¹³ C- ¹³ C with RFDR then PAR mixing	17.6 T (WB)	17.241	1.86 then 12.8	25	227.2
uCN	3D ¹⁵ N- ¹³ CA- ¹³ CX with PAR mixing	11.7 T (WB)	22.222	12.7	10	446
uCN	1D ¹³ C with fsREDOR mixing	11.7 T (WB)	11.111	1.8, 5.4, 9.0, 10.8	N/A	1.4
uDCN	3D ¹³ CA- ¹⁵ N- ¹ H	17.6 T (WB)	33.333	N/A	N/A	44.1
uDCN	3D ¹³ CO- ¹⁵ N- ¹ H	17.6 T (WB)	33.333	N/A	N/A	66.5
uDCN	3D ¹³ CA- ¹³ CO- ¹⁵ N- ¹ H with RFDR mixing	17.6 T (WB)	33.333	1.92	12.5	37.2
uDCN	3D ¹³ CO- ¹³ CA- ¹⁵ N- ¹ H with RFDR mixing	17.6 T (WB)	33.333	1.92	12.5	57.8
uDCN	3D ¹³ CA- ¹⁵ N- ¹ H- ¹ H with RFDR mixing	17.6 T (WB)	33.333	7.68	N/A	41.5
uDCN	3D ¹³ CA- ¹ H- ¹ H- ¹⁵ N- ¹ H with RFDR mixing	17.6 T (WB)	33.333	7.68	N/A	59.1
uDCN	3D ¹⁵ N- ¹ H- ¹ H- ¹⁵ N- ¹ H with RFDR mixing	17.6 T (WB)	33.333	7.68	N/A	97.8
uDCN	4D ¹ H- ¹⁵ N- ¹ H- ¹ H- ¹⁵ N- ¹ H with RFDR mixing	17.6 T (WB)	33.333	7.68	3	85.2
uDCN	2D ¹³ CA- ¹³ CO with CTUC-COSY mixing	17.6 T (WB)	33.333	9.6	N/A	7.1
uDCN	2D ¹³ Cali- ¹³ Cali with fpRFDR mixing	11.7 T (WB)	33.333	11.78	N/A	43.5
Diluted, (25% ^{2-¹³C Gly, ¹⁵N)}	2D ¹³ C- ¹³ C with DARR mixing	11.7 T (WB)	11.111	500	N/A	277.9
Diluted, (25% ^{2-¹³C Gly, ¹⁵N)}	2D ¹⁵ N- ¹³ CA	11.7 T (WB)	11.111	N/A	N/A	16.3
Diluted, (25% ^{2-¹³C Gly, ¹⁵N)}	2D ¹⁵ N- ¹³ CO	11.7 T (WB)	11.111	N/A	N/A	18.7
					Total Time	2750

Supplementary Table 10: ^{13}C , ^{15}N , and $^1\text{H}^{\text{N}}$ chemical shift assignments for LBD derived Asyn fibrils

Residue	$^1\text{H}^{\text{N}}$	^{15}N	$^{13}\text{C}'$	^{13}CA	^{13}CB	^{13}CG	^{13}CD	^{13}CE	^{13}CZ	$^{15}\text{ND}/^{15}\text{NE}/^{15}\text{NZ}$
--	--	--	--	--	--	--	--	--	--	--
K34	7.46	125.5	174.5	56.1	-	-	-	-	-	-
E35	8.76	121.9	176.3	53.4	35.7	35.6	183.4			
G36	8.75	117.5	173.6	48.4						
V37	7.67	118.6	172.4	60.0	35.7	21.9/24.5				
L38	8.88	127.8	173.8	52.6	47.3	27.5	25.3/29.0			
Y39	8.39	131.3	173.9	56.3	43.4	128.0	133.0	117.5	157.3	
V40	8.76	127.1	173.8	60.0	34.4	19.9/22.1				
G41	9.08	111.6	170.2	44.7						
S42	8.94	116.9	175.4	56.5	68.7					
K43	7.96	123.4	176.6	56.6	-	-	-	-	-	-
--	--	--	--	--	--	--	--	--	--	--
V49	-	-	-	-	-	-	-	-	-	-
H50	-	-	175.8	51.7	31.5	125.1	129.4	140.3		-/-
--	--	--	--	--	--	--	--	--	--	--
E61	-	-	173.1	-	-	-	-	-	-	-
Q62	8.15	122.6	174.3	54.5	-	-	-	-	-	-
V63	8.96	124.6	173.9	61.2	35.5	21.1/-				
T64	9.32	124.8	172.3	60.8	68.5	23.4/23.4				
N65	9.61	126.5	173.0	51.9	42.0	174.4				113.9
V66	9.32	125.0	177.0	59.9	34.4	20.9/23.0				
G67	8.83	112.6	171.9	47.4						
G68	6.07	100.7	172.1	44.4						
A69	8.74	121.8	175.0	50.0	22.1					
V70	8.95	124.5	175.8	61.7	32.7	19.7/21.2				
V71	9.18	131.0	173.9	61.3	34.7	19.7/22.1				
T72	9.28	124.7	174.6	60.1	71.4	22.5				
G73	8.96	117.8	172.1	49.0						
V74	7.73	117.6	173.8	59.4	37.4	20.3/23.3				
T75	8.86	123.4	171.8	61.7	68.8	22.9				
A76*	9.55	131.2	174.2	49.7	21.7					
V77*	8.76	122.4	172.2	60.6	36.7	20.6/25.1				
A78	9.17	130.3	175.7	50.7	23.1					
Q79	8.80	122.6	174.1	54.6	37.6	34.7	179.3			112.4
K80	8.97	126.5	173.9	54.7	-	-	-	-	-	-
T81	8.53	124.7	172.8	61.9	69.9	21.1				
V82	9.42	127.0	175.4	60.1	-	-/-				
E83	8.93	118.3	175.9	55.3						
G84	8.96	124.4	175.0	49.8						
A85	9.13	124.7	174.5	49.9	-					
G86	8.86	110.3	172.5	44.2						
S87*	9.46	119.7	174.4	56.4	67.4					
I88*	8.96	128.2	173.2	60.1	44.4	27.8/17.6	16.9			
A89	8.97	129.1	175.2	50.3	22.5					
A90	9.31	126.3	174.4	49.7	22.2					
A91	8.73	123.7	175.4	50.3	23.2					
T92	8.79	117.3	173.3	61.2	70.8	20.5				
G93	-	116.8	170.3	44.9						
F94	9.16	129.0	173.1	56.9	43.5	137.4	131.2	129.3	140.3	
V95	9.00	128.5	173.0	60.9	35.6	-/-				
K96	8.99	129.0	175.1	54.5	-	-	-	-	-	-
--	--	--	--	--	--	--	--	--	--	--

(*) Two sets of shifts observed for at least one atom in the residue. Primary shift is reported here.

Supplementary Table 11: Summary of simulated annealing protocols in the PASD algorithm

	pass 2	pass 3,4,5
<i>High temperature phase I</i>		
Duration (ps)	2	5
k_{lin} (kcal/mol/Å)	1	0
k_{quad} (kcal/mol/Å ²)	0	3
k_{repul} (kcal/mol/Å)	5	5
$\square r_c$ (Å)	∞	∞
w_p	1	1
Number of NOE re-evaluations	64	64
Number of MC steps	25	25
k_{nb} (kcal/mol/Å ⁴)	0	0.004
s_{nb}		1.2
Nonbonded interactions	None	C□-C□ only
$k_{R_{\text{gyr}}}$ (kcal/mol/Å ³)	0.001	0.001
k_{dihed} (kcal/mol/radians ²)	200	10
k_{tDB} (kcal/mol)	0.002	0.002
<i>High temperature phase II</i>		
Duration (ps)	6	
k_{lin} (kcal/mol/Å)	1	
k_{quad} (kcal/mol/Å ²)	0	
k_{repul} (kcal/mol/Å)	5	
$\square r_c$ (Å)	10	
w_p	0.5	
Number of NOE re-evaluations	64	
Number of MC steps	25	
k_{nb} (kcal/mol/Å ⁴)	0	
s_{nb}		
Nonbonded interactions	None	
$k_{R_{\text{gyr}}}$ (kcal/mol/Å ³)	0.001	
k_{dihed} (kcal/mol/radians ²)	200	
k_{tDB} (kcal/mol)	0.002	
<i>Cooling phase</i>		
Duration (ps)	250	250
k_{lin} (kcal/mol/Å)	1 → 30	0
k_{quad} (kcal/mol/Å ²)	0	3 → 30
k_{repul} (kcal/mol/Å)	5	5
$\square r_c$ (Å)	10 → 2	2 → 0.7
w_p	0.5 → 0	0.5 → 0
Number of NOE re-evaluations	128	128
Number of MC steps	100	100
k_{nb} (kcal/mol/Å ⁴)	0.004 → 1	0.004 → 1
s_{nb}	2.0	2.0
Nonbonded interactions	All atoms	All atoms
$k_{R_{\text{gyr}}}$ (kcal/mol/Å ³)	0.001 → 1.25	0.001 → 1.25
k_{dihed} (kcal/mol/radians ²)	200	10 → 300
k_{tDB} (kcal/mol)	0.002 → 2	0.002 → 2

Supplementary Table 12: Summary of Final Refinement Statistics.

NMR Distance and Dihedral Constraints	
Distance Restraints	
Total	1118
Manually Derived Restraints	45
PASD Derived Restraints	1073
Total Dihedral Angle Restraints	
Phi	46
Psi	46
Structure Statistics from Top 10	
<i>Violations</i>	
Distance Constraints (Å)	1.1 ± 0.9
Dihedral (°)	0.7 ± 0.6
<i>Deviations from Idealized Geometry</i>	
Bond Lengths (Å)	0
Bond Angles (°)	0
Impropers (°)	0
<i>Average Pairwise RMS deviation</i>	
Heavy Atom (Å)	1.7
Backbone (Å)	1.2

^aPairwise RMS deviation was calculated among the structured residues 35 – 46 and 62 – 96. Residues 47 – 61 are disordered.

References

1. Comellas, G. & Rienstra, C.M. Protein structure determination by magic-angle spinning solid-state NMR, and insights into the formation, structure, and stability of amyloid fibrils. *Annu Rev Biophys* **42**, 515-36 (2013).
2. Higman, V.A. Solid-state MAS NMR resonance assignment methods for proteins. *Prog Nucl Magn Reson Spectrosc* **106-107**, 37-65 (2018).
3. Barclay, A.M. et al. ¹³C and ¹⁵N resonance assignments of alpha synuclein fibrils amplified from Lewy Body Dementia tissue. *Biomolecular NMR Assignments* **17**, 281-286 (2023).
4. Barclay, A.M., Dhavale, D.D., Courtney, J.M., Kotzbauer, P.T. & Rienstra, C.M. Resonance assignments of an α -synuclein fibril prepared in Tris buffer at moderate ionic strength. *Biomol NMR Assign* **12**, 195-199 (2018).
5. Comellas, G., Lopez, J.J., Nieuwkoop, A.J., Lemkau, L.R. & Rienstra, C.M. Straightforward, effective calibration of SPINAL-64 decoupling results in the enhancement of sensitivity and resolution of biomolecular solid-state NMR. *Journal of Magnetic Resonance* **209**, 131-135 (2011).
6. Zhou, D.H. & Rienstra, C.M. High-performance solvent suppression for proton detected solid-state NMR. *J Magn Reson* **192**, 167-72 (2008).
7. Shen, Y. & Bax, A. Protein backbone and sidechain torsion angles predicted from NMR chemical shifts using artificial neural networks. *J Biomol NMR* **56**, 227-41 (2013).
8. Bayro, M.J. et al. Dipolar truncation in magic-angle spinning NMR recoupling experiments. *J Chem Phys* **130**, 114506 (2009).
9. De Paëpe, G., Lewandowski, J.R., Loquet, A., Böckmann, A. & Griffin, R.G. Proton assisted recoupling and protein structure determination. *J Chem Phys* **129**, 245101 (2008).
10. Colvin, M.T. et al. Atomic Resolution Structure of Monomorphic A β 42 Amyloid Fibrils. *J Am Chem Soc* **138**, 9663-74 (2016).
11. Takegoshi, K., Nakamura, S. & Terao, T. ¹³C–¹H dipolar-assisted rotational resonance in magic-angle spinning NMR. *Chemical Physics Letters* **344**, 631-637 (2001).
12. Li, S., Zhang, Y. & Hong, M. 3D (¹³C)-(¹³C)-(¹³C) correlation NMR for de novo distance determination of solid proteins and application to a human alpha-defensin. *J Magn Reson* **202**, 203-10 (2010).
13. Bennett, A.E., Griffin, R.G., Ok, J.H. & Vega, S. Chemical shift correlation spectroscopy in rotating solids: Radio frequency-driven dipolar recoupling and longitudinal exchange. *The Journal of Chemical Physics* **96**, 8624-8627 (1992).
14. Bennett, A.E. et al. Homonuclear radio frequency-driven recoupling in rotating solids. *The Journal of Chemical Physics* **108**, 9463-9479 (1998).
15. Rienstra, C.M., Hohwy, M., Hong, M. & Griffin, R.G. 2D and 3D ¹⁵N–¹³C–¹³C NMR Chemical Shift Correlation Spectroscopy of Solids: Assignment of MAS Spectra of Peptides. *Journal of the American Chemical Society* **122**, 10979-10990 (2000).
16. Vuister, G.W. & Bax, A. Resolution enhancement and spectral editing of uniformly ¹³C-enriched proteins by homonuclear broadband ¹³C decoupling. *Journal of Magnetic Resonance (1969)* **98**, 428-435 (1992).
17. Baldus, M., Petkova, A.T., Herzfeld, J. & Griffin, R.G. Cross polarization in the tilted frame: assignment and spectral simplification in heteronuclear spin systems. *Molecular Physics* **95**, 1197-1207 (1998).
18. Zambrello, M.A. et al. Nonuniform sampling in multidimensional NMR for improving spectral sensitivity. *Methods* **138-139**, 62-68 (2018).

19. Paramasivam, S. et al. Enhanced sensitivity by nonuniform sampling enables multidimensional MAS NMR spectroscopy of protein assemblies. *J Phys Chem B* **116**, 7416-27 (2012).
20. Hoch, J.C., Maciejewski, M.W., Mobli, M., Schuyler, A.D. & Stern, A.S. Nonuniform Sampling in Multidimensional NMR. in *eMagRes* (2012).
21. Jaroniec, C.P., Tounge, B.A., Herzfeld, J. & Griffin, R.G. Frequency Selective Heteronuclear Dipolar Recoupling in Rotating Solids: Accurate ^{13}C - ^{15}N Distance Measurements in Uniformly ^{13}C , ^{15}N -labeled Peptides. *Journal of the American Chemical Society* **123**, 3507-3519 (2001).
22. Tran, Hien T. et al. α -Synuclein Immunotherapy Blocks Uptake and Templated Propagation of Misfolded α -Synuclein and Neurodegeneration. *Cell Reports* **7**, 2054-2065 (2014).
23. Bhattacharjee, P. et al. Mass Spectrometric Analysis of Lewy Body-Enriched α -Synuclein in Parkinson's Disease. *J Proteome Res* **18**, 2109-2120 (2019).
24. Kellie, J.F. et al. Quantitative measurement of intact alpha-synuclein proteoforms from post-mortem control and Parkinson's disease brain tissue by intact protein mass spectrometry. *Sci Rep* **4**, 5797 (2014).
25. Li, W. et al. Aggregation promoting C-terminal truncation of alpha-synuclein is a normal cellular process and is enhanced by the familial Parkinson's disease-linked mutations. *Proc Natl Acad Sci U S A* **102**, 2162-7 (2005).
26. Giasson, B.I. et al. Neuronal alpha-synucleinopathy with severe movement disorder in mice expressing A53T human alpha-synuclein. *Neuron* **34**, 521-533 (2002).